Homepage of Andreas Dörnbrack in collaboration with Thomas Birner

---

ECMWF Analyses

Arctic Polar Vortex

T and Z on P- Levels

PV on Isentropes

Tropopause Maps (NH)

Rahmen enthielt PDF-Datei. Klicken Sie hier für Anzeige

Potential Temperature
Horizontal Wind
Pressure
Geopotential Height
Temperature
Water Vapor
Ozon

Tropopause Maps (SH)

Potential Temperature
Horizontal Wind
Pressure
Geopotential Height
Temperature
Water Vapor
Ozon

PV on Middleworld Isentropes

290 K
310 K
330 K
350 K
375 K

Current Date and Time are:
Thu, 09 Mar 2006
16:30:22 GMT

Previous Campaign Forecasts

Scandinavia (SOLVE I & II, EUPLEX)

Spitzbergen (ASTAR)

Germany (Persistent Contrails) see **PAZI-LAUNCH**

Startpage

designed 2004 by **Marci Strausz** and **Andreas Dörnbrack**

Mountain Wave–Induced Polar Stratospheric Cloud Forecasts for Aircraft Science Flights during SOLVE/THESEO 2000

STEPHEN D. ECKERMANN,* ANDREAS DÖRNBRACK,+ SIMON B. VOSPER,# HARALD FLENTJE,+ M. J. MAHONEY,@ T. PAUL BUI,& AND KENNETH S. CARSLAW**

*E. O. Hulburt Center for Space Research, Naval Research Laboratory, Washington, DC
+DLR, Oberpfaffenhofen, Germany
#Met Office, Exeter, United Kingdom
@Jet Propulsion Laboratory, California Institute of Technology, Pasadena, California
&Atmospheric Chemistry and Dynamics Branch, NASA Ames Research Center, Moffett Field, California
**School of the Environment, University of Leeds, Leeds, United Kingdom

(Manuscript received 17 December 2004, in final form 8 August 2005)

ABSTRACT

The results of a multimodel forecasting effort to predict mountain wave–induced polar stratospheric clouds (PSCs) for airborne science during the third Stratospheric Aerosol and Gas Experiment (SAGE III) Ozone Loss and Validation Experiment (SOLVE)/Third European Stratospheric Experiment on Ozone (THESEO 2000) Arctic ozone campaign are assessed. The focus is on forecasts for five flights of NASA's instrumented DC-8 research aircraft in which PSCs observed by onboard aerosol lidars were identified as wave related. Aircraft PSC measurements over northern Scandinavia on 25–27 January 2000 were accurately forecast by the mountain wave models several days in advance, permitting coordinated quasi-Lagrangian flights that measured their composition and structure in unprecedented detail. On 23 January 2000 mountain wave ice PSCs were forecast over eastern Greenland. Thick layers of wave-induced ice PSC were measured by DC-8 aerosol lidars in regions along the flight track where the forecasts predicted enhanced stratospheric mountain wave amplitudes. The data from these flights, which were planned using this forecast guidance, have substantially improved the overall understanding of PSC microphysics within mountain waves. Observations of PSCs south of the DC-8 flight track on 30 November 1999 are consistent with forecasts of mountain wave–induced ice clouds over southern Scandinavia, and are validated locally using radiosonde data. On the remaining two flights wavelike PSCs were reported in regions where no mountain wave PSCs were forecast. For 10 December 1999, it is shown that locally generated mountain waves could not have propagated into the stratosphere where the PSCs were observed, confirming conclusions of other recent studies. For the PSC observed on 14 January 2000 over northern Greenland, recent work indicates that nonorographic gravity waves radiated from the jet stream produced this PSC, confirming the original forecast of no mountain wave influence. This forecast is validated further by comparing with a nearby ER-2 flight segment to the south of the DC-8, which intercepted and measured local stratospheric mountain waves with properties similar to those predicted. In total, the original forecast guidance proves to be consistent with PSC data acquired from all five of these DC-8 flights. The work discussed herein highlights areas where improvements can be made in future wave PSC forecasting campaigns, such as use of anelastic rather than Boussinesq linearized gridpoint models and a need to forecast stratospheric gravity waves from sources other than mountains.

1. Introduction

To study processes responsible for Arctic stratospheric ozone loss, two major planned field campaigns were combined during the Arctic winter of 1999/2000. The U.S. component was the National Aeronautics and Space Administration (NASA) sponsored SAGE III Ozone Loss and Validation Experiment (SOLVE), the acronym referring to the additional goal of acquiring suborbital validation data for the third Stratospheric Aerosol and Gas Experiment (SAGE III) on the *Meteor-3M* spacecraft. Unfortunately, the launch of *Meteor-3M* was delayed until December 2001, leading

Corresponding author address: Stephen D. Eckermann, E. O. Hulburt Center for Space Research, Code 7646, Naval Research Laboratory, Washington, DC 20375.
E-mail: stephen.eckermann@nrl.navy.mil

SOLVE to focus more on the stratospheric science goals. The European component was the European Commission sponsored Third European Stratospheric Experiment on Ozone (THESEO 2000). More than 500 scientists participated in SOLVE/THESEO 2000. Activities were coordinated from the Arena Arctica hangar at Kiruna airport, in northern Sweden (68°N, 20°E), where six instrumented research aircraft were based and operated at various times during the campaign. Newman et al. (2002) provide a comprehensive overview of SOLVE/THESEO 2000, including goals, logistics, implementation, and some initial research highlights.

Science flights studying ozone loss processes require careful planning to acquire the requisite scientific data using available onboard instruments and to maximize their overall scientific impact. For example, following the discovery of an "ozone hole" over Antarctica, NASA DC-8 and ER-2 research aircraft acquired stratospheric data during the Airborne Antarctic Ozone Experiment (AAOE) of August–October 1987 that helped confirm one of the several competing theories for its formation: namely, enhanced photochemical ozone destruction by free chlorine radicals supplied by anthropogenic chlorofluorocarbon emissions (Solomon 1999). The success of AAOE owed much to careful flight planning, based in large measure on stratospheric forecast fields issued by operational global numerical weather prediction (NWP) models. NWP fields, once available, were postprocessed into specialized AAOE mission products, such as isentropic potential vorticity maps and parcel trajectories, which were used to devise flight tracks along isentropes or to resample air measured during earlier flights (Tuck et al. 1989). During the 1990s, progressively higher resolution global NWP model forecasts played important and more elaborate roles in flight planning for subsequent airborne measurement campaigns focusing on ozone loss in both the Arctic and Antarctic stratospheres (Wofsy et al. 1994; Pyle and Harris 1995; Stefanutti et al. 1999a; Newman et al. 1999). As understanding of the chemistry associated with polar ozone loss improved, forecast winds from global NWP models were interfaced to global chemical transport models (CTMs) to provide stratospheric chemical forecasts for some later missions prior to SOLVE/THESEO 2000 (e.g., Lee et al. 1997). In preparation for SOLVE/THESEO 2000, it was clear that accurate daily forecasts of the meteorology of the polar stratosphere would once again be essential for scientific flight planning (Newman et al. 2002).

The importance of stratospheric meteorology for these ozone-focused missions is due not just to transport, but also to the strong control that dynamics exert on stratospheric temperatures. The progressive chlorine activation within and denitrification of stratospheric air that lead to rapid ozone loss in sunlight occur within polar stratospheric clouds (PSCs). PSCs only form where temperatures are very cold ($\lesssim$190–195 K), and the geographical location and depth of these coldest temperatures are controlled mostly by synoptic-scale stratospheric meteorology. Thus, airborne measurements of PSCs and their attendant chemistry and microphysics require accurate forecasts of vortex meteorology to vector flights into geographical zones where temperatures are cold enough for PSCs to exist.

The meteorology of the polar winter stratosphere is characterized by a strong symmetric vortex circulation, which isolates cold polar air from midlatitudes. Planetary waves episodically propagate upward from tropospheric sources, displacing and distorting the vortex and enhancing descent, which warms the stratosphere adiabatically (Newman and Nash 2000). Global models capture these dynamics quite well: indeed, global NWP models have better forecast skill in the stratosphere than the troposphere during polar winter, permitting relatively accurate predictions several days or more into the future (Waugh et al. 1998; Lahoz 1999). While much finer-scale structure is often observed in ozone and related chemicals, CTM studies have shown that this is often the result of isentropic advection by this large-scale meteorology, which can be simulated quite accurately with high-resolution offline trajectories driven by coarser-resolution winds from the global models (see, e.g., Newman et al. 1996).

For these reasons, finer-scale stratospheric dynamics (e.g., gravity waves) were of limited interest when planning flights during early airborne stratospheric ozone campaigns and, so, were not specifically forecast. This situation differs markedly from the troposphere, where mesoscale and planetary-scale circulations both significantly influence chemistry and microphysics (e.g., Webster and Houze 1991; Jacob et al. 2003).

Things began to change during the mid- to late 1990s when polar ozone research focused on the Arctic. Greater topography in the Northern Hemisphere generates stronger planetary wave activity, leading to a more disturbed Arctic vortex and, hence, generally warmer wintertime stratospheric temperatures that exhibit much greater intraseasonal and interannual variability than those in the Antarctic (Pawson and Naujokat 1999; Newman et al. 2001). The warmer Arctic stratosphere produces fewer PSCs and less ozone-loss chemistry (Chipperfield and Jones 1999; Randel and Wu 1999), explaining to first order why the huge losses that yield an ozone hole only occur in the Antarctic.

Yet ozone loss can still be significant in the Arctic. Prior to SOLVE/THESEO 2000, some state-of-the-art global CTM runs were systematically underpredicting the wintertime ozone loss that was observed during previous Arctic winters, due to insufficient PSC formation within the models (e.g., Lutman et al. 1997; Becker et al. 1998). Intercomparisons of minimum stratospheric temperatures in Arctic winter from various global analysis systems, while revealing substantial differences on occasion, did not show any clear systematic warm bias in analysis compared to observations that might explain this PSC underprediction (Knudsen et al. 2002; Manney et al. 2003). This suggested instead that important additional PSC formation mechanisms might be missing from the models.

At about the same time, the role of finer-scale stratospheric dynamics on PSCs and ozone chemistry began receiving serious attention. European aircraft campaigns out of Kiruna during the mid- to late 1990s repeatedly measured PSCs that formed in the cooling phases of stratospheric mountain waves generated by flow across the Scandinavian Mountains (Carslaw et al. 1998b; Wirth et al. 1999). While mountain waves had been observed forming PSCs in earlier airborne Antarctic missions (Cariolle et al. 1989), their effect proved secondary because of the much more extensive synoptic-scale decks of PSC produced by very cold intravortex temperatures. Conversely, minimum synoptic temperatures in the Arctic often hover at or just above the threshold for PSC formation (Schulz et al. 2001). Thus, temperature decreases due to subsynoptic mountain waves could be a much more significant source of PSCs in the Arctic. Since global models generally cannot resolve mountain wave dynamics (see below), Carslaw et al. (1998a) argued that unresolved mountain waves might be the missing ingredient needed in global CTMs to form more PSCs, leading to greater Arctic ozone loss in better agreement with observations. Using a high-resolution global model, Edouard et al. (1996) showed that unresolved small-scale variability in reactive chemical species could have very large influences on modeled Arctic ozone loss. On analyzing aircraft data from earlier missions, Sparling et al. (1998) estimated that unresolved variability in ClO could lead to underestimates in ozone loss near the edge of the Arctic vortex of ~5%–35%.

Thus, leading up to SOLVE/THESEO 2000 there was new interest in mountain wave–induced PSCs as a priority scientific measurement goal requiring forecasting. Unfortunately, during 1999–2000 the U.S. global NWP models were running at ~1° horizontal resolution (~100 km). Since the very smallest spatial scales in global spectral models are unreliable (Lander and Hoskins 1997), model orography is smoothed and spectral divergence damping is imposed to suppress wave forcing at these scales (Derber et al. 1998) so that only at horizontal wavelengths ~6–10 times this minimum gridpoint resolution of ~100 km would one expect predictive skill (Davies and Brown 2001; Skamarock 2004). Since mountain waves have horizontal wavelengths ~5–500 km, forecasts from global NWP systems were not expected to resolve any significant mountain wave activity for SOLVE/THESEO 2000.

Thus, other forecasting approaches were necessary. It soon became clear that no single model could provide the necessary mountain wave predictive capabilities for this campaign. Section 2 describes the three different models that were ultimately used to predict mountain wave–induced PSCs for aircraft flight planning during SOLVE/THESEO 2000. The forecasting effort was carefully planned and successfully executed (see section 2.4 of Newman et al. 2002). In the ~6 yr that have transpired since, the PSC community has completed and published initial scientific analyses of the PSC data acquired by the aircraft, identifying measured clouds that appear to be mountain wave related (Hu et al. 2002; Dörnbrack et al. 2002; Luo et al. 2003; Fueglistaler et al. 2003; Svendsen et al. 2005). Here we compare the wave PSCs identified in lidar data from the DC-8 and Falcon research aircraft with the models' original forecast guidance. Section 3 describes instruments on the aircraft that acquired PSC and meteorological data that we use to validate our wave PSC forecasts. Detailed comparisons between the models' mountain wave PSC predictions and available PSC and wave measurements are given in section 4. Results are summarized in section 5, along with some recommendations for future mission forecasting.

2. Mountain wave models and forecasting

a. Requirements for PSC forecasting

The mandate of this forecasting effort was to predict the geographical locations, horizontal extents, and altitudes of mountain wave–induced PSCs, to aid flight planning for the scientific research aircraft. Stratospheric mountain waves that did not produce PSCs (e.g., Hertzog et al. 2002) were of limited interest to flight planners.

There are three different types of PSCs: type Ia, consisting of nitric acid trihydrate (NAT) particles; type Ib, consisting of supercooled ternary ($HNO_3/H_2SO_4/H_2O$) solution (STS) droplets; and type II, consisting of water ice particles. At a given altitude each PSC type has a formation threshold temperature, denoted T_{NAT}, T_{STS}, or T_{ICE}. If stratospheric temperatures drop below these

TABLE 1. Properties of mountain wave models used for high-resolution stratospheric forecasting during SOLVE/THESEO 2000.

Model	Geographical domain	Vertical range[a]	Used to predict wave-induced . . .	Initialization/boundary fields[b]	Forecast range (h)
MWFM	SOLVE AAO[c] (relocatable)	1000–10 hPa	$T < T_{NAT}$, T_{ICE},[d] turbulence	NCEP AVN/MRF, NOGAPS, GMAO	0–120 h
MM5	Scandinavia (Δx = 24 km)	0–27 km	$T < T_{NAT}$, T_{ICE},[d] wind changes[e]	ECMWF IFS	24–84 h
3DVOM	Spitzbergen, northern Scandinavia (Δx = 2 km)	0–28 km	$T < T_{NAT}$, T_{ICE}[d]	ECMWF IFS	24–84 h

[a] For SOLVE/THESEO 2000, model fields were output on a smaller subset of upper-tropospheric and stratospheric levels.
[b] See Table 2 for more details on these models.
[c] Area of airborne operations; see Fig. 1. MWFM forecasts were frequently relocated to focus on specific regions within the AAO, or to encompass wider domains extending outside the AAO; e.g., during ferry flights between Kiruna and U.S. air bases.
[d] That is, wave-induced temperature perturbations that drop local temperatures T below thresholds T_{NAT} and T_{ICE} for formation of type I and II PSCs, respectively.
[e] Wave-induced changes in stratospheric streamlines were used to plan quasi-Lagrangian PSC measurement flights.

thresholds, PSCs of this type can exist. Since $T_{NAT} > T_{STS} > T_{ICE}$, type I PSCs are most likely to form, whereas type II PSCs require the very coldest stratospheric temperatures and are least common. For typical stratospheric mixing ratios of H_2O and HNO_3 of 5 ppmv and 10 ppbv, respectively (Toon et al. 1989), the 30-hPa NAT point temperature T_{NAT} ~193 K (Hanson and Mauersberger 1988), while the frost point temperature T_{ICE} ~186 K (Marti and Mauersberger 1993). Thus, the models had to predict accurately geographical locations and altitudes where mountain waves dropped stratospheric temperatures below these representative T_{NAT} and T_{ICE} thresholds.

After preparatory premission meetings, three models were chosen because of their complementary capabilities in forecasting mountain wave–induced stratospheric temperature variability. The models and their forecasting configurations are summarized in Table 1, and each is described in depth in sections 2c–2e. The Mountain Wave Forecast Model (MWFM) provided rapid hemispheric forecasts of stratospheric mountain wave temperature amplitudes and wave-induced turbulence potential. The fifth-generation Pennsylvania State University–National Center for Atmospheric Research Mesoscale Model (MM5) provided detailed forecasts of long-wavelength mountain wave–induced stratospheric temperature variability over Scandinavia, as well as streamlines for planning quasi-Lagrangian flights along forecast particle trajectories (e.g., Wirth et al. 1999). The Vosper Orographic Model (3DVOM) provided high-resolution forecasts of shorter-wavelength mountain wave–induced temperature variability in the stratosphere near Kiruna (and later over Spitzbergen). In a loose sense, these three models provided a kind of nested forecasting capability, with forecasts over the Arctic by MWFM supplemented with additional resolution and detail from MM5 and 3DVOM over Scandinavia and Kiruna, the base for airborne operations.

b. Global NWP models

The starting point for all stratospheric forecasting during SOLVE/THESEO 2000 was global ground-to-stratosphere forecasts and analyses issued operationally by meteorological centers in both the United States and Europe. In addition to being inspected regularly to assess the forecast evolution of synoptic-scale stratospheric temperatures and potential vorticity, these fields provided initial conditions for the mountain wave forecasting models. The specific global NWP model forecasts and analyses that were used to initialize the mountain wave models are summarized in Table 2. Many other forecast/analysis fields were also utilized in other ways during SOLVE/THESEO 2000: see Table 7 of Newman et al. (2002).

c. MWFM

The MWFM is an diagnostic postprocessor of NWP model winds and temperatures that provides regional or global forecasts of mountain wave properties at specifiable atmospheric pressure levels. MWFM mountain wave–induced turbulence forecasts have been used primarily as a flight planning safety tool for high-altitude long-endurance aircraft during previous NASA science campaigns and by the U.S. Department of Defense (Bacmeister et al. 1994; Newman et al. 1999; Eckermann 2002; Eckermann et al. 2004). For SOLVE/THESEO 2000, the MWFM was extended to predict mountain wave temperature amplitudes $\hat{T}_{PEAK}$ for PSC forecasting.

TABLE 2. Properties of global fields issued by numerical weather prediction models, used as initial/boundary conditions for mountain wave forecasting models in Table 1.

Global NWP system	No. of levels[a]	Top pressure level (hPa)[a]	Horizontal resolution (°)[a]	Vertical coordinate	Forecast hours (UTC)[a]
GMAO forecast[b]	36	0.2	2.5×2	σ	0000, 1200
GMAO analysis[c]	36	0.2	1×1	σ	0000, 0600, 1200, 1800
ECMWF IFS[d]	21	1	0.5×0.5	hybrid $\sigma - p$	0000, 0600, 1200, 1800
NCEP forecast[e]	14	10	1×1	σ	0000, 1200
NCEP analysis[e]	14	10	1×1	σ	0000
NOGAPS[f]	16	10	1×1	σ	0000, 1200

[a] These values refer to the standard gridded spatial output on reference pressure levels that we accessed from these model runs and do not, in general, represent the intrinsic ranges and resolutions of the models themselves.
[b] NASA's Global Modeling and Assimilation Office (GMAO) GEOS-3 GCM was run in forecast mode during SOLVE/THESEO 2000 (Newman et al. 2002).
[c] Both "first look" (FLK) and "late look" (LLK) GEOS-3 DAS analyses were used based on a $1° \times 1°$ L48 model; for details on GEOS-2.8 DAS, see Dee and Todling (2000) and references therein.
[d] Based on operational forecast and analysis output from the $T_L319L60$ ECMWF IFS that went operational on 12 Oct 1999 (Jakob et al. 2000).
[e] Two NCEP forecasts were accessed: an early Aviation Model (AVN) forecast, and a later Medium-Range Forecast (MRF) model. Both models ran at T126L28 prior to 24 Jan 2000, and at T170L42 thereafter (Caplan and Pan 2000), using the operational statistical spectral interpolation (SSI) analysis system (Parrish and Derber 1992).
[f] Operational T159L24 model NOGAPS forecasts (Hogan and Rosmond 1991) and analyses using the navy's multivariate optimum interpolation (MVOI) system (Barker 1992).

1) MWFM SURFACE FORCING

A list of quasi-two-dimensional (2D) ridges characterizes the dominant features in the earth's topography relevant for the MWFM mountain wave calculations. Each ridge feature has, among other properties, a characteristic cross-ridge width L, peak height h, base height z_b, and horizontal orientation φ_{LONG} of its long axis. These parameters define the properties of mountain waves generated by surface flow over these orographic features. Bacmeister et al. (1994) and Eckermann et al. (2004) provide more information on the ridge databases.

Figure 1 shows two ridge databases available for use in the MWFM, one characterizing medium width ridges of $L \sim$35–150 km (top plot), the other capturing narrower ridges with $L \sim$20–70 km (lower plot). Note that many ridges lie on top of one another, since this ridge-finding procedure progressively decomposes complex topography into a series of overlapping and overlaying ridge functions, with narrow-width ridges typically isolating peaks that sit atop broader-width ridges defining larger-scale topography. These properties are reflected, for example, in each ridge's base altitude z_b, which can be several kilometers above sea level if the identified ridge feature characterizes a peak sitting atop a broader ridge feature with a lower z_b.

Winds, temperatures, and geopotential heights from operational NWP models are ingested on pressure levels and used to specify forecast flow conditions at the "surface" of the ridge, z_s. From wind speeds $|U(z_s)|$ and Brunt–Väisälä frequencies $N(z_s)$, the inverse Froude number $Fr^{-1} = N(z_s)h/|U(z_s)|$ is computed. If $Fr^{-1} > 1$, we assume that the flow here is either blocked upstream of this ridge (if it is a 2D feature) or diverted around it (if it is a more 3D feature); either way, the flow at z_s does not pass over the ridge and generate gravity waves. We then compute the reduced component of the ridge height $\tilde{h} < h$ that forces a gravity wave using an Fr-dependent procedure described in the appendix. This final ridge elevation $\hat{h}$ and other ridge properties are used to specify amplitudes and wavelengths of the mountain wave generated at z_s.

2) MWFM-1

Two versions of the MWFM were run during SOLVE/THESEO 2000. Both use the same ridge databases, but different types of wave equations to model the forcing, propagation, and breakdown of the mountain waves by the forecast flow profiles over these ridges.

Version 1 of the MWFM (MWFM-1) is described by Bacmeister et al. (1994) and Eckermann et al. (2004). It uses hydrostatic irrotational gravity wave equations under the assumption that a single linear plane (2D) mountain wave is forced by the surface flow component parallel to the short axis of each ridge feature. A number of minor changes to this original MWFM-1 formulation accumulated prior to SOLVE/THESEO 2000. One important upgrade was to replace earlier pressure-based approximations of atmospheric density scaling

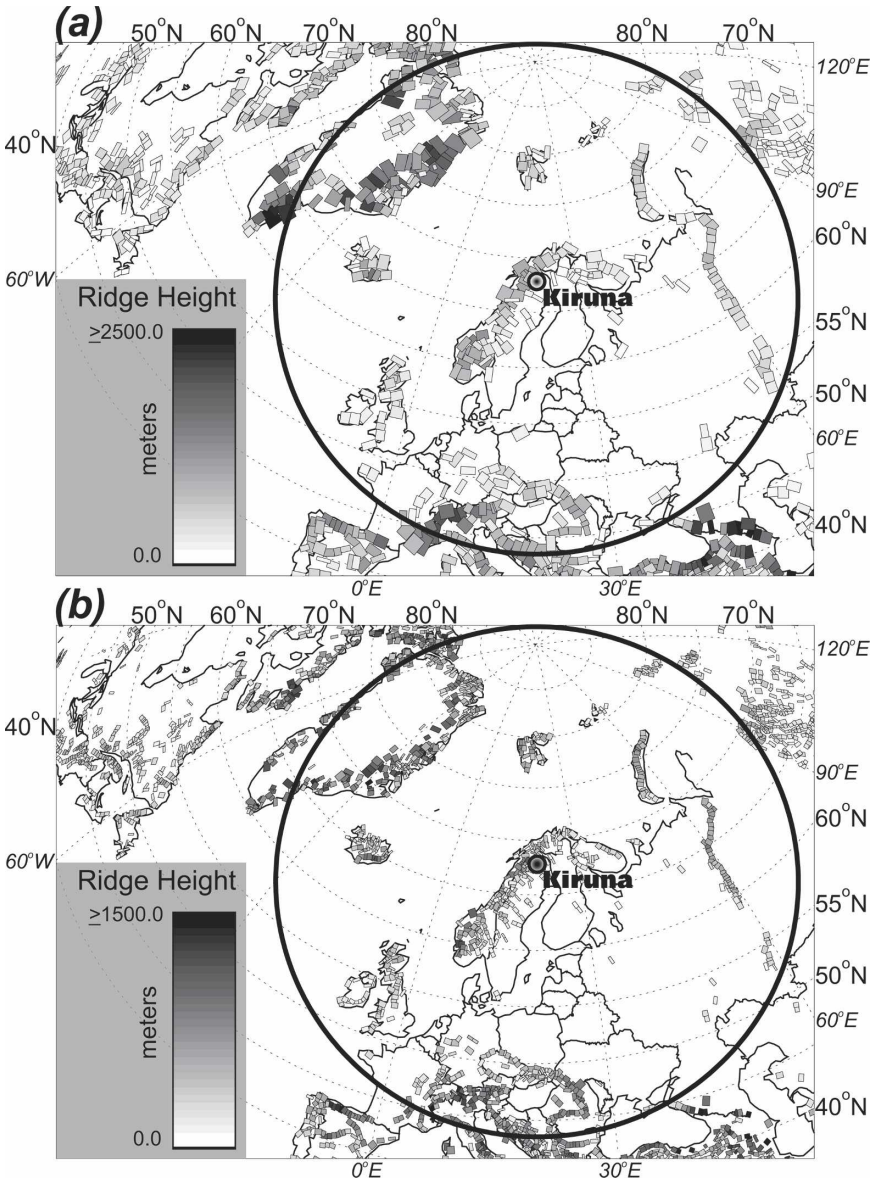

FIG. 1. MWFM ridge databases showing (a) medium- and (b) small-width ridges, with elevations shaded and orientations depicted. In both plots the ridges are sorted in order of descending elevation, with low-elevation ridges plotted on top of higher-elevation ridges, consistent with smaller peaks sitting atop larger ones. Circle depicts the perimeter of the nominal SOLVE area of airborne operations (AAO), defined as distances ≤2700 km from Kiruna (Newman et al. 2002).

terms in the momentum flux calculations with atmospheric densities computed directly from input pressure and temperature profiles.

3) MWFM-2

For SOLVE/THESEO 2000, we issued forecasts for the first time using a next-generation, version 2, MWFM (MWFM-2). Eckermann and Preusse (1999) presented first results from an initial research version developed prior to SOLVE/THESEO 2000, preliminarily validated against satellite data. MWFM-2 has since been developed and used in many subsequent studies, where its evolving formulations are described in more depth (Hertzog et al. 2002; Jiang et al. 2004; Pagan et al. 2004; Eckermann et al. 2004). Here we review its status and salient features for SOLVE/THESEO 2000 forecasting.

MWFM-2 replaces the two-dimensional irrotational hydrostatic gravity wave equations used in MWFM-1

with a set of three-dimensional ray-tracing equations governed by a nonhydrostatic dispersion relation with rotation of the form (Marks and Eckermann 1995)

$$m^2 = \frac{(k^2 + l^2)(N^2 - \omega^2)}{\omega^2 - f^2} - \frac{1}{4H_\rho^2}, \quad (1)$$

where (k, l, m) is the wavenumber vector, ω is intrinsic frequency, f is the inertial frequency, and H_ρ is density scale height. The ray implementation in MWFM-2 maintains as much backward compatibility with MWFM-1 as possible, while including new features. Wave amplitudes are calculated using constancy of vertical flux of wave action density $c_{gz}A$ along individual rays in the absence of dissipation, where A is wave action density and c_{gz} is vertical group velocity. Wave breaking is identified using threshold amplitudes for convective and dynamical instabilities (Fritts and Rastogi 1985), and is parameterized using a wave saturation hypothesis. The final formulation is similar to that outlined by Marks and Eckermann (1995). One difference is that temporal rates of change and horizontal gradients in background winds and temperatures are not included explicitly in the ray equations. Under these approximations, ground-based horizontal phase speeds remain stationary ($c_h = 0$) and horizontal wavenumber vectors $\mathbf{K}_h = (k, l)$ remain constant along ray group trajectories.

Unlike MWFM-1, which launches a single ray from each ridge, MWFM-2 launches a total of I individual rays from each ridge with different horizontal wavenumbers $(\mathbf{K}_h)_i = (k_i, l_i)$ and horizontal propagation azimuths $\varphi_i = \arctan(l_i/k_i)$, where the subscript $i = 1, \ldots, I$ tags each ray. The general approach to ray initialization at the source height z_s is explained in detail in section 4.1 of Jiang et al. (2004), and the specifics for SOLVE/THESEO 2000 are summarized in the appendix.

The new nonhydrostatic MWFM-2 ray formulation offered some significant potential improvements for wave PSC forecasting. Previous MWFM-1 simulations of stratospheric mountain waves tended to be "overactive"; that is, wave amplitudes were generally too large compared to other estimates (e.g., Carslaw et al. 1998b, 1999), which could lead to false-alarm wave PSC forecasts. One likely source of this overactivity was the MWFM-1 hydrostatic irrotational wave equations, which do not simulate vertical reflections at turning points z_t where ω approaches the high-frequency cutoff $\omega_c \sim N$ (see Marks and Eckermann 1995), allowing waves that should be vertically trapped within the troposphere to enter the stratosphere. The nonhydrostatic MWFM-2 ray equations identify rays that reflect vertically (Marks and Eckermann 1995). While ray methods can be used to model these trapped waves (Schoeberl 1985; Broutman et al. 2003), for SOLVE/THESEO 2000 we simply removed rays that reached turning points before entering the stratosphere, since we were only interested in stratospheric mountains waves and this quick removal helped speed up the forecasts. Test MWFM forecasts prior to SOLVE/THESEO 2000 confirmed that peak mountain wave temperature amplitudes predicted by MWFM-2 were lower and within a more realistic range than corresponding MWFM-1 predictions. Thus, MWFM-2 forecasts were our primary MWFM-based guidance for wave PSC forecasts, with MWFM-1 providing backup and cross-validation support.

4) Forecasting configuration

To provide a crude ensemble forecasting capability, MWFM issued separate forecasts initialized with fields from each of the three U.S. global models issuing ground-to-stratosphere forecasts at the time. One set of MWFM forecasts was initialized using global NWP fields issued by the National Centers for Environmental Prediction (NCEP) Aviation (AVN) and Medium-Range Forecast (MRF) models (Kanamitsu 1988). Another was initialized using fields from the Navy Operational Global Atmospheric Prediction System (NOGAPS) run at the Fleet Numerical Meteorology and Oceanography Center (FNMOC) (Hogan and Rosmond 1991). A third MWFM forecast was initialized using output from the GEOS-3 gridpoint global model and Data Assimilation System (DAS) (Swinbank et al. 1999; Dee and Todling 2000), which ran in a reduced-resolution operational forecasting mode during SOLVE/THESEO 2000 at what was then known as NASA's Data Assimilation Office and is now the Global Modeling and Assimilation Office (GMAO). MWFM-1 and MWFM-2 forecasts were both issued in each case.

Since MWFM was the only one of the three mountain wave forecasting models capable of issuing forecasts over the entire Arctic, its standard forecast maps covered the entire SOLVE area of airborne operations, depicted in Fig. 1, at standard reference pressure levels in the 10–100-hPa range. These MWFM forecasts ran automatically at set times each day (staggered based on various global NWP model output times) at the Naval Research Laboratory (NRL) in Washington, D.C. Tailored forecasts for specific scientific or flight planning needs were devised and run quickly in the field when required.

The main forecast maps used by flight planners were MWFM-2 forecasts of stratospheric mountain wave

peak temperature amplitudes, $\hat{T}_{\mathrm{PEAK}}$. These ray amplitudes were superimposed onto contours of forecast background temperatures T from the global NWP model, to help flight planners visually locate regions where $T - \hat{T}_{\mathrm{PEAK}}$ dropped below T_{NAT} or T_{ICE} and thus PSCs of types I or II, respectively, might form. MWFM also forecast the locations and intensities of turbulence due to mountain wave breaking, as a flight-planning safety tool for NASA's DC-8 and high-altitude ER-2 research aircraft (Eckermann et al. 2000, 2004), since previous in situ sampling of mountain wave PSCs near Kiruna with a high-altitude European aircraft encountered substantial turbulence within these waves (Stefanutti et al. 1999b).

d. MM5

The MM5 (Dudhia 1993; Grell et al. 1994) was set up at the Deutsches Zentrum für Luft- und Raumfahrt e.V. (DLR) in Oberpfaffenhofen, Germany, to generate operational forecasts of stratospheric mountain waves over Scandinavia. MM5 uses a finite-difference approximation to solve the fully compressible, nonhydrostatic set of fluid equations in a rotating frame of reference. Due to computational limitations, of all the possible parameterizations available in the model to represent physical processes (e.g., radiation, convection), only a turbulence scheme was used. Thus, the model ran "dry" in stratospheric forecast mode at DLR. The model used 52 levels (σ coordinates) from the ground to 10 hPa, where a radiation boundary condition minimized any spurious downward reflection of vertically propagating gravity waves. The aforementioned model setup was first used at DLR to forecast stratospheric mountain waves over Scandinavia during the winter of 1996/97 (Dörnbrack et al. 1998), verifying its utility for mountain wave PSC forecasting near Kiruna.

For SOLVE/THESEO 2000, the model was configured into a set horizontal domain of 92×92 grid cells centered at 65°N and 15°E with horizontal mesh sizes $\Delta x = \Delta y = 24$ km, which spanned all of Scandinavia, as shown later (Fig. 6c). Higher-resolution runs could not be performed, as only 16 CPUs on a CRAY J90 supercomputer were available for the forecasts at DLR.

Forecasts were initialized using +24-h forecast fields from the European Centre for Medium-Range Weather Forecasts (ECMWF) Integrated Forecast System (IFS) 1200 UTC forecast runs (see Table 2) at 15 selected pressure levels. Lateral boundary conditions within the MM5 model were updated every 6 h using subsequent 6-hourly ECMWF forecast fields, so that MM5 boundary conditions at model forecast times of +6 and +12 h were given by the +30-h and +36-h ECMWF forecast fields, respectively. Each MM5 forecast was run out to +60 h. The total CPU time for a complete forecast cycle, including both pre- and post-processing, was ~60 h.

These forecasts ran automatically without significant interruptions at DLR from 1 December 1999 until mid-March of 2000. Final forecast products were regularly available at 0600 UTC on the mission Web server. The main maps of interest to flight planners were stratospheric temperatures at given pressure levels, cross sections of temperatures along possible flight segments, and winds and streamlines for planning quasi-Lagrangian flights measuring PSCs along forecast particle trajectories.

e. 3DVOM

1) MODEL FORMULATION

The 3DVOM is a finite-difference three-dimensional numerical model designed for high-resolution simulations of mountain waves generated by flow over complex terrain. The model is described in detail by Vosper (2003) and Vosper and Worthington (2002), who used it to simulate tropospheric mountain waves over the United Kingdom.

The 3DVOM is based on the time-dependent linearized equations of motion for a dry atmosphere. The equations of motion are linearized about a background wind and potential temperature field (assumed to be dependent on height only) and are integrated forward in time until a steady wave field is obtained. The version of 3DVOM that was used for operational forecasts during SOLVE/THESEO 2000 is based on the shallow Boussinesq version of the equations (Dutton and Fichtl 1969). Although generally valid for tropospheric waves, when a greater depth of the atmosphere is considered, the Boussinesq approximation can give rise to wave amplitude errors (Nance and Durran 1994) in the stratosphere. Thus, the model was extended after SOLVE/THESEO 2000 to an anelastic equation set derived by Lipps and Hemler (1982), which yields more accurate wave solutions over depths of several density scale heights (Nance and Durran 1994).

The linearized form of both equation sets can be written as follows:

$$\frac{\partial \tilde{\mathbf{u}}}{\partial t} + \overline{\mathbf{U}} \cdot \boldsymbol{\nabla}_h \tilde{\mathbf{u}} + \tilde{w} \frac{\mathrm{d}\overline{\mathbf{U}}}{\mathrm{d}z} + a \boldsymbol{\nabla} \tilde{\pi} - \frac{g\tilde{\theta}}{\overline{\theta}} \mathbf{k} = 0, \qquad (2)$$

$$\frac{\partial \tilde{\theta}}{\partial t} + \overline{\mathbf{U}} \cdot \boldsymbol{\nabla}_h \tilde{\theta} + \tilde{w} \frac{\mathrm{d}\overline{\theta}}{\mathrm{d}z} = 0, \qquad (3)$$

and

$$\nabla \cdot \tilde{\mathbf{u}} + d\frac{\tilde{w}}{\overline{\rho}}\frac{\mathrm{d}\overline{\rho}}{\mathrm{d}z} = 0, \tag{4}$$

where

$$(u', v', w', \theta', \pi') = b(\tilde{u}, \tilde{v}, \tilde{w}, \tilde{\theta}, c\tilde{\pi}). \tag{5}$$

In the above, $\nabla_h = (\partial/\partial x, \partial/\partial y)$, $\mathbf{k} = (0, 0, 1)$, $\mathbf{u}' = (u', v', w')$ is the wave perturbation velocity vector, θ' is the potential temperature perturbation, and $\overline{\rho}(z)$, $\overline{\theta}(z)$ and $\overline{\mathbf{U}}(z)$ are the background density, potential temperature, and horizontal velocity vector, respectively. For forecasting, these background profiles are taken from global NWP model output. The definition of π and the values of the coefficients a, b, c, and d depend on whether the Boussinesq approximation is made or the Lipps–Hemler equation set is used. Details are given in Table 3.

The model equations are discretized on a staggered mesh using a second-order-accurate centered finite-difference scheme. Steady wave solutions are obtained by integrating (2) and (3) forward in time (from an initial state in which no waves are present) using a modified leapfrog scheme. At each time step a Poisson equation is solved for $\tilde{\pi}$, which ensures that mass continuity (4) is satisfied. A free-slip lower-boundary condition is applied and zero perturbation conditions are imposed at the upper and side boundaries. Rayleigh damping is applied below the upper boundary to absorb upward-propagating waves. Similarly, damping is applied near all side boundaries to minimize wave reflection. In both cases the damping is increased linearly from zero to a maximum value at the boundaries.

2) Forecasting configuration

High-resolution 3DVOM forecasts were performed using a 256 km × 256 km horizontal domain centered near Kiruna (see Fig. 2). Forecasts here were issued daily between 4 December 1999 and 15 March 2000. These forecasts were designed to provide very high-resolution information about the temperature amplitudes of shorter-wavelength (nonhydrostatic) mountain waves that are not resolved by the coarser-resolution MM5 forecasts over Scandinavia. Previous lidar observations of PSCs had shown wavy signals within the clouds themselves, with wavelengths often as short as 10–20 km (Carslaw et al. 1998b; Wirth et al. 1999), which can make a significant contribution to local cooling and PSC evolution.

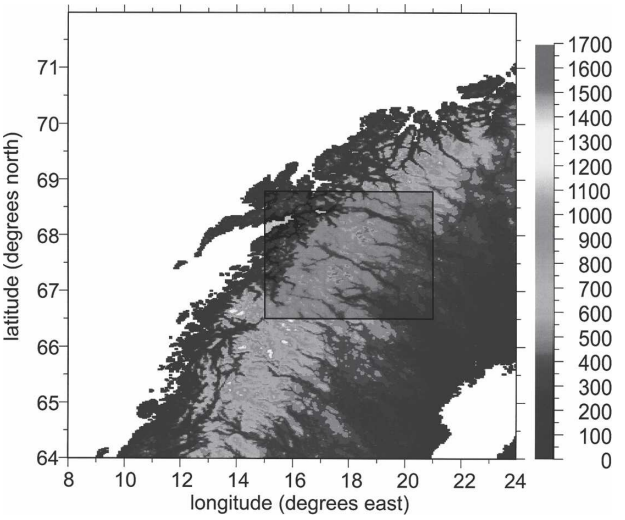

FIG. 2. The northern Scandinavian mountains (terrain heights in m). Rectangle shows boundaries of the computational domain used by 3DVOM for SOLVE/THESEO 2000 forecasts.

The horizontal and vertical grid spacings used for the forecasts were $\Delta x = \Delta y = 2$ km and $\Delta z = 650$ m, respectively. The model upper boundary was placed at 40 km and Rayleigh damping was imposed above 28 km. Daily mountain wave forecasts were generated using a vertical profile of winds, densities, and potential temperatures at 68°N, 18°E (the center of the model domain) from ECMWF IFS forecasts. The model equations were integrated forward in time for approximately 2.2 h, by which time a quasi-steady mountain wave field was generally established. Each day the model was run four times to predict wave fields at 1200 UTC (a 24-h forecast), 0000 UTC the following day (a 36-h forecast), and 0000 UTC 2–3 days ahead (60- and 84-h forecasts, respectively). Forecasts were run on a Silicon Graphics Origin 2000 system at the University of Leeds and graphical output was generated and transferred to the mission Web server. The first of the daily forecasts was usually completed by 0800 UTC.

Extra daily forecasts were set up over the island of Spitzbergen (79°N, 18°E) for the period 15 December 1999–15 March 2000, where the coldest climatological stratospheric temperatures are centered (Newman et al. 2002) and mountain waves can often form (Skeie and Grønås 2000). The domain size and grid spacings were the same as for the Scandinavia forecasts. Due to

TABLE 3. Parameter settings for Boussinesq and anelastic versions of 3DVOM. Entries provide the definition of π and the values of the coefficients in (2)–(5). Here, p is the pressure, p_0 is a reference pressure (10^3 hPa), c_p is the specific heat capacity at constant pressure, and R is the gas constant for dry air.

Model	a	b	c	d	π
Boussinesq	1	$\overline{\rho}^{-1/2}$	$\overline{\rho}$	0	p
Lipps–Hemler	c_p	1	$\overline{\theta}^{-1}$	1	$(p/p_0)^{R/c_p}$

constraints on computing time, only two forecasts were generated for Spitzbergen each day. These were valid at 1200 UTC on successive days (24- and 48-h forecasts).

3. Aircraft validation data

To validate forecasts of mountain wave–induced PSCs, we use data acquired by instruments on three of the six aircraft operated during SOLVE/THESEO 2000.

a. Aerosol lidar data from the NASA DC-8 and DLR Falcon

We use high-resolution PSC data acquired remotely by two similar lidar profilers operated on two aircraft flying near the tropopause. The Langley Research Center (LaRC) aerosol lidar operated on the NASA DC-8 during SOLVE/THESEO 2000 in comanifested form with the Goddard Space Flight Center Airborne Raman Ozone and Temperature lidar. The LaRC lidar emits laser pulses at 1064, 532, and 355 nm, the fundamental, doubled, and tripled frequencies, respectively, from a neodymium:yttrium/aluminum/garnet laser. The Ozone Lidar Experiment (OLEX) (Flentje et al. 2000), operated from the DLR Falcon F-20 aircraft, uses these same laser wavelengths. Both systems transmit vertically and collect backscattered radiation with zenith-viewing telescopes for processing.

We focus solely on aerosol backscatter ratios (ABRs) derived from lidar backscatter at 1064 nm:

$$S_{1064} = \frac{\beta_{\text{aerosol}} + \beta_{\text{air}}}{\beta_{\text{air}}}, \tag{6}$$

where β_{air} and β_{aerosol} are the backscatter coefficients from air and aerosol molecules, respectively. The lidar measures the total backscatter $\beta_{\text{aerosol}} + \beta_{\text{air}}$: β_{air} is derived using atmospheric densities from meteorological analyses along track. Final LaRC lidar ABRs are issued at 75-m vertical resolution every ~15 s.

Stratospheric ABRs provide first-order discrimination among different PSC types. PSC-free regions yield S_{1064} ~1, type I PSCs (NAT/STS) yield S_{1064} ~3–30, and type II PSCs (ice) yield S_{1064} ~50–500 (e.g., Fueglistaler et al. 2003).

b. Meteorological measurements from the NASA ER-2

We utilize meteorological stratospheric data from two instruments that operated autonomously on NASA's ER-2 research aircraft during SOLVE/THESEO 2000. The ER-2 cruises typically at 50–70 hPa.

The Meteorological Measurement System (MMS) acquires in situ measurements of the three-component wind velocity, temperature, and pressure (Scott et al. 1990). Raw 10-Hz data were averaged to 1 Hz to improve signal to noise, which, for a nominal ER-2 true airspeed of 200 m s^{-1}, yields ~200 m resolution along track. Bacmeister et al. (1996) have shown that the small-scale variability in 1-Hz MMS stratospheric velocities and temperatures is dominated by gravity waves.

We also utilize data from the Microwave Temperature Profiler (MTP) (Denning et al. 1989). The ER-2 MTP retrieves a temperature profile several kilometers above and below the aircraft from line-of-sight radiances from two pairs of O_2 rotational lines observed at a series of different elevation angles. Final profiles are issued every 10 s. We convert temperature profiles into potential temperatures by using MTP-issued background atmospheric number densities to derive pressure profiles from the ideal gas equation.

4. Forecasts of mountain wave–induced PSCs

To provide an observational focus for objectively assessing our mountain wave PSC forecasts, we concentrate on PSC data acquired from the NASA DC-8. Using LaRC aerosol lidar data as their guide, Hu et al. (2002) reviewed all the DC-8 flight data during SOLVE/THESEO 2000 and identified four flights in which LaRC S_{1064} data showed values and structure that led them to a mountain wave PSC interpretation.

Here we assess the forecasts for all four of these flight dates, since they provide a good range of situations for assessment. Two of these flights, on 23 and 25 January 2000, were meticulously planned based on the models' predictions of wave PSCs over eastern Greenland and Scandinavia, respectively. Conversely, the other two flights of 10 December 1999 and 14 January 2000 were not planned with wave PSCs in mind, since models predicted no mountain wave PSCs, yet wavelike enhancements in S_{1064} were observed nonetheless. These cases are particularly important to study and reconcile.

A wave PSC was also observed indirectly from the DC-8 on 30 November 1999. We begin by studying this case before progressing to the other four flights.

a. 30 November 1999: PSCs over southern Scandinavia

1) FORECASTS

Stratospheric mountain wave forecasting was just starting up on 30 November 1999 as the NASA DC-8 completed its ferry flight from Dryden Flight Research Center (DFRC) in California to Kiruna to commence

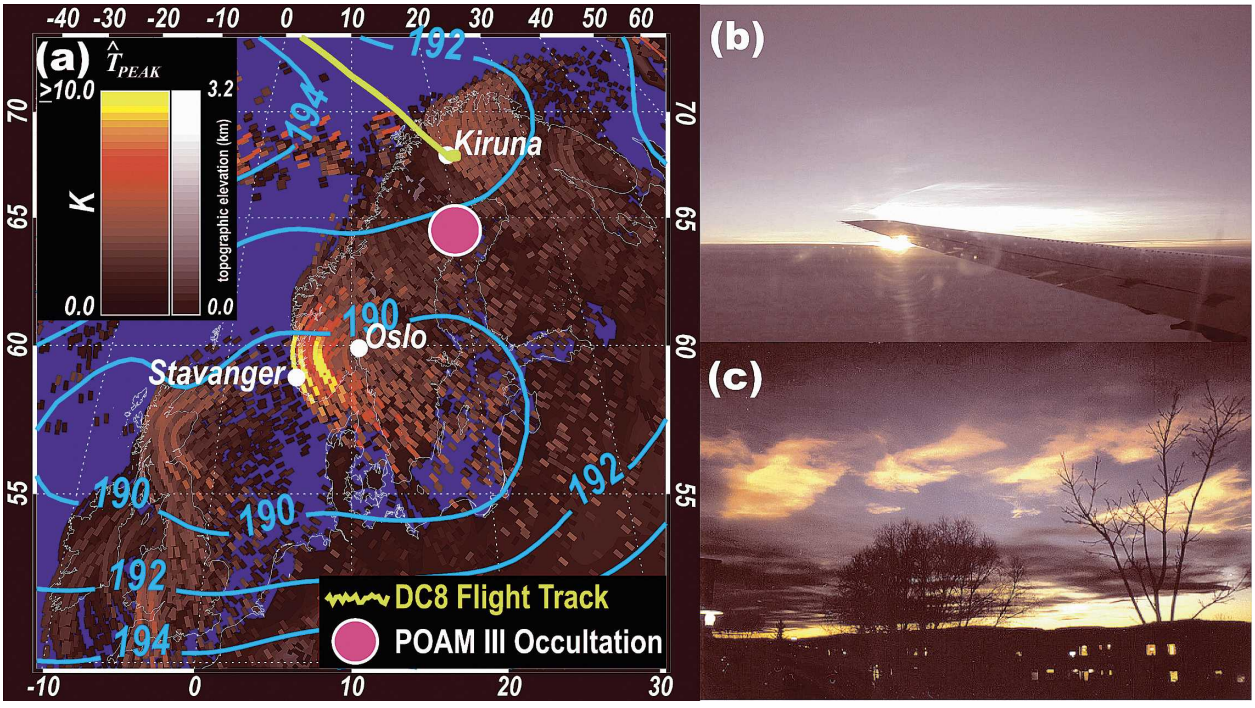

FIG. 3. (a) The +18-h MWFM-2 forecast of peak temperature amplitudes $\hat{T}_{\mathrm{PEAK}}$ of mountain waves at 30 hPa on 30 Nov 1999 at 1800 UTC, based on operational NOGAPS forecasts from FNMOC. Blue contours show NOGAPS 30-hPa forecast temperatures, red-yellow pixels show peak mountain wave temperature amplitudes, both in K. Each pixel shows the location and amplitude of a forecast mountain wave ray group, and values are plotted in order of ascending amplitude, with larger-amplitude ray pixels plotted on top of smaller-amplitude ones. Color bar scales are linear. Topographic elevations are shaded in grayscale beneath the ray pixels. Pink circle shows the ground-level location of the POAM III PSC detection on this day; green curve shows the flight track of the NASA DC-8 into Kiruna. (b) Photograph from the NASA DC-8 (taken by M. Schoeberl, NASA Goddard Space Flight Center) on 30 Nov 1999 at ~1000 UTC. Cirruslike PSCs are visible in the distance to the south above the DC-8 wingtip. (c) Photograph (taken by G. Braathen, Norwegian Institute for Air Research in Oslo) of iridescent banded PSCs over southern Norway at dusk on 1 Dec 1999. Note that the tropospheric clouds in the lower foreground are relatively dark since the sun has set on these lower-altitude clouds.

the first phase of SOLVE/THESEO 2000. On this day, only MWFM was issuing operational forecasts: MM5 forecasts commenced the following day.

Figure 3a shows the plot of the MWFM-2 +18-h forecast of mountain wave–induced peak temperature amplitudes $\hat{T}_{\mathrm{PEAK}}$ at 30 hPa, valid on 30 November 1999 at 1800 UTC, based on initialization by operational NOGAPS +18-h forecasts from FNMOC initialized at 0000 UTC on this day. NOGAPS predicted a broad region of very cold 30-hPa temperatures T below ~190 K over Scotland and southern Scandinavia: see blue contours in Fig. 3a. Similar features emerged in NCEP and GMAO forecasts, although temperatures were a little warmer (see also Hood et al. 2001). Figure 3a shows that the MWFM-2 predicted peak mountain wave temperature amplitudes of up to ~5–10 K over southern Scandinavia within the core of these low synoptic temperatures. These waves can drop local temperatures ($T - \hat{T}_{\mathrm{PEAK}}$) below T_{ICE} ~186 K, and thus mountain wave–induced type II PSCs were forecast to form in this region.

2) OBSERVATIONAL VALIDATION

As the DC-8 circled to land at Kiruna airport (green flight track in Fig. 3a), mission scientists on board visually observed thick iridescent PSCs well to the south: a photograph of these clouds from the DC-8 is shown in Fig. 3b. A type I PSC detection was reported by the orbiting Polar Ozone and Aerosol Measurement (POAM) III instrument at the location shown in Fig. 3a, as well as at other locations in the days before and after (Hood et al. 2001). The following day, spectacular banded PSCs were visible from the ground near Oslo, Norway, and were again photographed (Fig. 3c). The strong banding evident in the PSCs in Fig. 3c is a fingerprint of clouds formed in the cooling phases of a gravity wave, and strongly suggests that local stratospheric mountain wave activity was controlling their formation and microphysical evolution. Their excellent visibility to remote photography suggests high opacity, strongly suggesting type II ice PSCs. Thus, these visual observations are consistent with the MWFM-NOGAPS

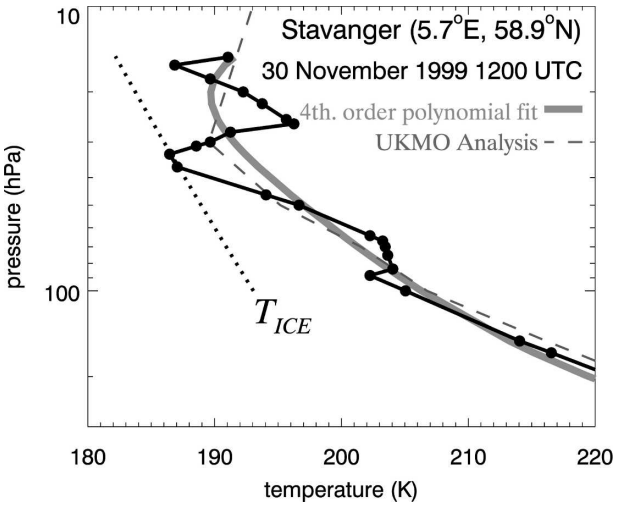

FIG. 4. Filled circles connected by solid curve show temperatures from a radiosonde launched from Stavanger, Norway (see Fig. 3a), on 30 Nov 1999 at 1200 UTC. The thick light-gray curve shows a least squares fourth-order polynomial fit to the entire profile. The dashed gray curve shows closest gridbox profile from the 1200 UTC Met Office analysis. Dotted black curve shows frost point temperatures T_{ICE} assuming 5.5 ppmv of stratospheric water vapor (Marti and Mauersberger 1993).

forecast in Fig. 3a of mountain wave–induced type II PSCs forming near Oslo.

As shown in Fig. 3a, Stavanger, Norway, is located near the region of largest predicted stratospheric wave amplitudes. The routine 1200 UTC radiosonde sounding from Stavanger on 30 November 1999 acquired winds and temperatures up to ~15 hPa. Assuming a typical ascent velocity of 5 m s^{-1} (e.g., Lane et al. 2000), trajectory calculations based on the radiosonde wind data place the balloon ~3° to the east and slightly south of Stavanger when it reached 30 hPa, which is within the region of large predicted MWFM-2 ray amplitudes in Fig. 3a

Figure 4 shows a plot of stratospheric temperatures acquired from this radiosonde ascent. At ~15–50 hPa a coherent wavelike oscillation with a peak amplitude ~5 K is evident, superimposed on background temperatures ~190 K. The radiosonde horizontal winds (not shown) also display a coherent stratospheric oscillation that is 90° out of phase with this temperature oscillation, consistent with polarization relations for a gravity wave. Thus, these data support the MWFM-2 forecast of mountain wave amplitudes of up to 5–10 K at 30 hPa, superimposed on background temperatures of ~189–190 K: see Fig. 3a. The wave oscillation drops temperatures in Fig. 4 below T_{ICE} within a narrow layer centered at ~35 hPa. This confirms the original forecast of synoptic temperatures too warm to form ice, but of ice forming in the cooling phases of mountain waves, further reinforcing the interpretation of the PSCs in Figs. 3b and 3c as mountain wave–induced type II. Given the extensive PSC displays, it suggests larger wave amplitudes at different locations and times than those in Fig. 4 that dropped temperatures within larger volumes further below T_{ICE}.

b. 25–27 January 2000: PSCs over northern Scandinavia

1) MWFM

Figure 5 shows MWFM-2 forecasts, using NOGAPS forecasts as initialization, of peak mountain wave temperature amplitudes $\hat{T}_{\mathrm{PEAK}}$ at 30 hPa over Scandinavia, all valid for 26 January 2000 at 1200 UTC, ranging in forecast time from +96 h down to +12 h. These plots depict the kind of evolving guidance these forecasts provided for in-field flight planning purposes.

Synoptic 30-hPa NOGAPS temperatures, overplotted as blue contours in Fig. 5, predicted very cold regions over northern Scandinavia, produced by a weak wave-1 disturbance that pushed the core of the coldest intravortex temperatures toward Scandinavia. We noted in the field, however, that NOGAPS stratospheric temperatures were sometimes systematically too cold compared to other NWP models by anywhere up to ~2–5 K. This is one such case. The origin of this cold bias is not clear, but may be related to poor vertical resolution in the stratosphere, a low 1-hPa model top, cold bias in the operational assimilation, and no parameterized nonorographic gravity wave drag (e.g., Shepherd 2000; Austin et al. 2003). Nonetheless, during SOLVE/THESEO 2000 we found that, apart from this episodic cold bias, NOGAPS prognostic tropospheric and lower-stratospheric meteorology compared quite well with that from other global NWP models. Thus, NOGAPS fields provided reliable initial meteorological conditions for MWFM mountain wave forecasting, so long as occasional systematic stratospheric temperature underpredictions were borne in mind when interpreting forecast maps like those in Fig. 5.

At +96 h (4 days out), MWFM-2 predicted strong mountain wave amplitudes over southern Scandinavia, with $\hat{T}_{\mathrm{PEAK}} \approx 10$ K, as well as a zone of weaker wave amplitudes to the north near Kiruna: see Fig. 5h. These and other forecasts provided advanced warning to flight planners of the potential for wave PSCs to form over Scandinavia in the coming days. Over the next 24 h, the MWFM-NOGAPS forecasts changed somewhat, with predicted wave amplitudes to the south weakening and those to the north intensifying, such that the +72-h forecast showed $\hat{T}_{\mathrm{PEAK}} \approx$ 8–10 K near Kiruna and

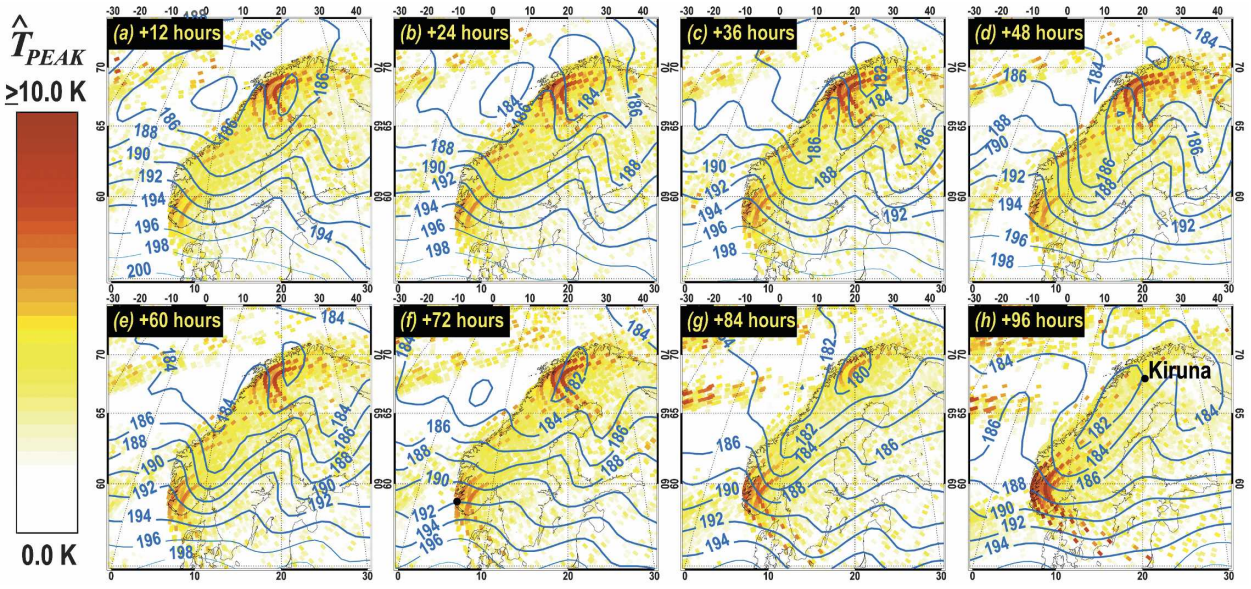

FIG. 5. Sequence of MWFM-2 forecasts of peak mountain wave temperature amplitudes $\hat{T}_{\mathrm{PEAK}}$ at 30 hPa over Scandinavia, valid for 26 Jan 2000 at 1200 UTC, based on successive operational NOGAPS forecasts from FNMOC, ranging from +4 days out [see (h)] down to +12 h out [see (a)]. Blue contours show NOGAPS 30-hPa forecast temperatures, and red-yellow pixels show peak mountain wave temperature amplitudes, both in K, as in Fig. 3a. Color bar scale is linear. Each pixel shows the location and amplitude of a forecast mountain wave ray group, and ray group pixels are arranged in order of ascending amplitude.

$\hat{T}_{\mathrm{PEAK}} \approx$ 6–8 K over southern Scandinavia. Thereafter, the MWFM-2 forecasts did not change substantially, continuing to show strong ~10 K mountain wave amplitudes over northern Scandinavia on 25–27 January. MWFM-2 forecasts initialized with NCEP AVN/MRF and GMAO GEOS-3 forecasts showed the same basic features, increasing confidence in the forecasts. Combined with the low predicted stratospheric temperatures near Kiruna, these forecasts predicted mountain wave type I–II PSCs forming over this region on 25–27 January.

2) MM5

Once early MWFM forecasts were predicting mountain wave PSCs over Scandinavia, MM5 forecasts received close scrutiny. DLR's MM5 forecasting was pioneered during earlier European campaigns in Scandinavia (Dörnbrack et al. 1998). Those forecasts had shown a stratospheric mountain wave response over the Scandinavian mountains that was often dominated by long horizontal wavelength waves that were well resolved by MM5 and thus could be forecast quite accurately.

MM5 forecasts valid for 1200 UTC 26 January 2000 predicted a large-amplitude long-wavelength (λ_h ~400 km) mountain wave propagating into the stratosphere over northern Scandinavia. The +24-h MM5 30-hPa temperature forecast is shown in Fig. 6b. Indeed, the vertical and horizontal wavelengths, λ_z and λ_h, were sufficiently long that this wave also appeared in global ECMWF IFS forecast temperatures, as shown in Fig. 6a. Just south of Kiruna, the forecast MM5 wave temperature oscillations were ~±9–10 K, yielding 30-hPa temperatures as low as 181 K (Fig. 6), some 5 K below the frost point. Thus, type II PSCs were forecast here. Wave temperature amplitudes in the ECMWF forecasts are ~50% smaller than MM5 near Kiruna, with a coldest forecast temperature ~184 K. The amplitude of the wave train downstream of Kiruna in ECMWF IFS is ~75% smaller than in MM5. Serious wave amplitude underpredictions also occurred in the final ECMWF analysis temperatures (Fueglistaler et al. 2003).

Dörnbrack et al. (2002) showed that the downstream penetration of this wave was due to inertial modifications caused by an intrinsic wave frequency $|\omega|$ near f, which in turn is a result of the long horizontal wavelength. Since shorter-λ_h mountain waves are simulated by MWFM-2 using its shorter-width ridge database over Scandinavia (Fig. 1), the waves it predicted had higher frequencies ($\omega^2 \gg f^2$) and thus did not leak downstream due to inertial effects: their limited downstream penetration in Fig. 5 is due mostly to "ship wake" effects due to wave radiation from three-dimensional ridge features.

The MM5 forecast in Fig. 6b also shows a weaker-

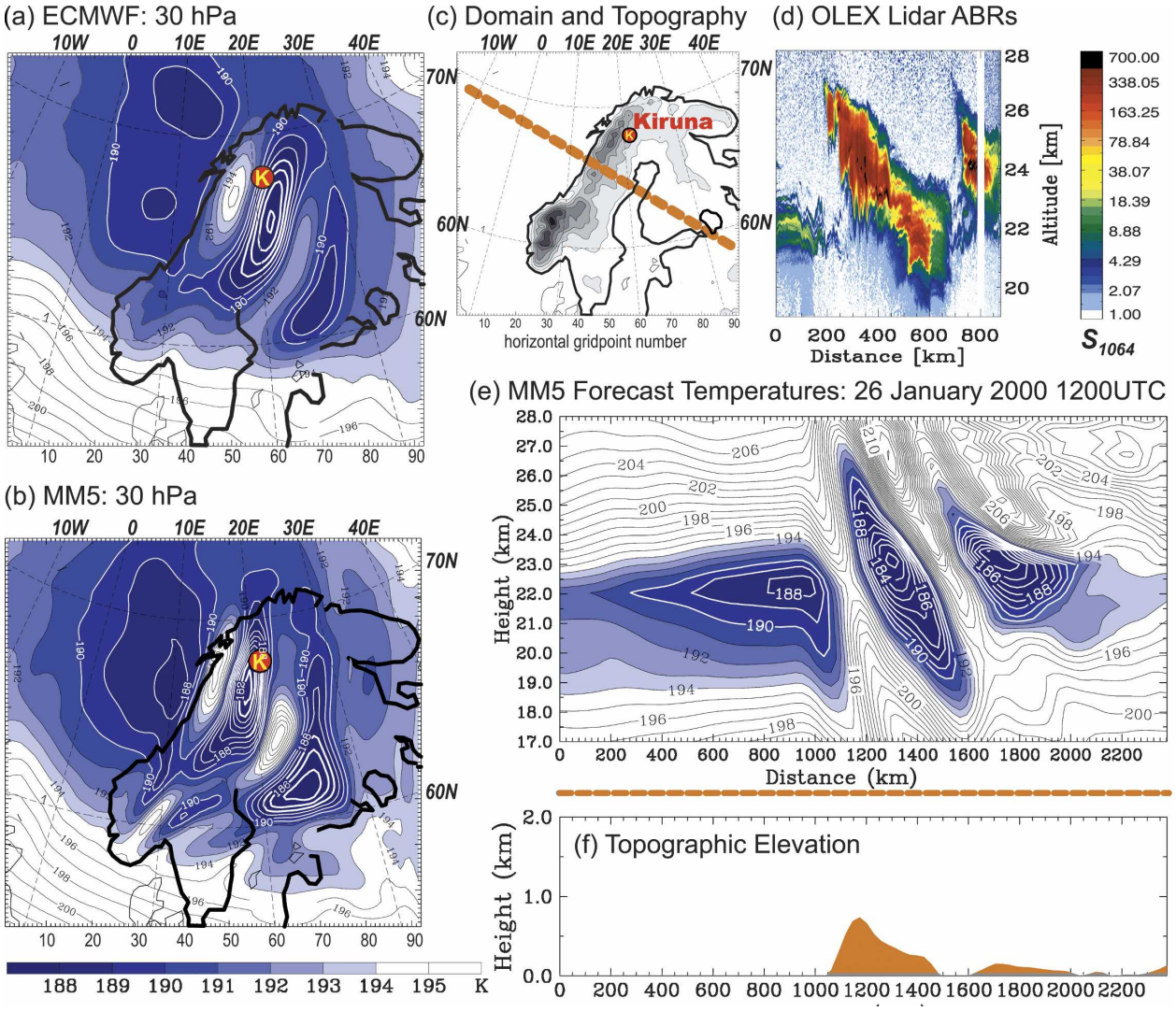

FIG. 6. The 24-h forecasts of 30-hPa stratospheric temperatures for 1200 UTC 26 Jan 2000 from (a) ECMWF IFS global forecasts and (b) MM5 mesoscale model forecasts. Tick marks show the 92 × 92 grid points used in the MM5 forecasts, location of Kiruna is shown with the white K in a red filled circle. Temperatures below a nominal 195-K threshold for NAT formation are shaded blue, with darker shading corresponding to colder temperatures. Temperatures below 190 K have white contours. (c) The MM5 regional domain and topography. (d) Plot of ABRs at 1064 nm, S_{1064}, from OLEX measurements from a DLR Falcon flight segment along part of the transect shown in (c). The thick linear dashed curve in (c) depicts a horizontal transect across Scandinavia, along which (e) the MM5 stratospheric temperature forecasts are profiled vertically, along with (f) the underlying topographic elevations.

amplitude mountain wave over southern Scandinavia with a much shorter horizontal wavelength. MM5 was expected to reliably forecast stratospheric gravity waves with horizontal wavelengths ≳150 km (≳6Δx): waves shorter than this were not reliably simulated (Leutbecher and Volkert 2000; Davies and Brown 2001; Skamarock 2004). Thus, the amplitude of this shorter-λ_h wave over southern Scandinavia was probably underestimated; indeed, the coarser-resolution ECMWF IFS forecast in Fig. 6a did not resolve it at all. Its amplitude in Fig. 6b is ~3 K, whereas the forecast MWFM-2 wave amplitudes over southern Scandinavia in Fig. 5a are ~5 K. In either case, the waves here were predicted to form type I but not type II PSCs.

Various Web site options allowed flight planners to profile these forecast temperature fields in various ways. One such view, depicted in Fig. 6c, was a two-dimensional linear transect that approximately followed a forecast 30-hPa streamline, as might be flown by an aircraft acquiring quasi-Lagrangian data (Wirth

et al. 1999). Figure 6e shows the two-dimensional forecast temperature cross section as a function of altitude and flight distance along this transect. Upstream of the Scandinavian mountains between ~19 and 23 km, synoptic temperatures are below T_{NAT} and so can support type I PSCs. Above and downstream of the mountains, cold regions form along the sloping phase of the forecast mountain wave, which descends from ~27 to ~18 km on progressing eastward, with the core of coldest temperatures of ~182 K at 23 km slightly downstream of the peak topography. Since these temperatures lie well below T_{ICE}, they can produce type II PSCs.

These and other MM5 forecast maps provided flight planners with extremely detailed information with which to plan science flights. On 26 January 2000, a planned DLR Falcon flight profiled various cold wave phases in these MM5 stratospheric temperature forecasts using OLEX, in hopes of measuring the predicted wave PSCs. Two west-to-east transects were flown, as well as two other transects along the mountains designed to track the coldest forecast phases of the wave.

One of the eastward flight segments flown by the Falcon was almost identical to the one shown in Fig. 6c. The 1064-nm OLEX ABRs, S_{1064}, from this flight segment are plotted in Fig. 6d (after Dörnbrack et al. 2002). As the Falcon flew from left to right in Fig. 6d, OLEX first measured S_{1064} ~10–30 at ~22 km, indicating type I PSCs consistent with $T_{ICE} < T < T_{NAT}$ at this altitude in the MM5 forecast. Farther along, two tilted layers containing $S_{1064} \gg 50$–100 reveal type II PSCs that correlate with temperatures below T_{ICE} in the cold phases of MM5's predicted mountain wave. Dörnbrack et al. (2002) used a more sophisticated lidar data classification scheme to argue that the thick core of enhanced backscatter is produced by type II ice particles, with type Ia and Ib particles surrounding the upper and lower edges of these ice layers (see also Fueglistaler et al. 2003).

3) 3DVOM

The MM5 and MWFM forecasts of mountain wave PSCs forming quite near Kiruna led us to focus on the high-resolution 3DVOM forecasts centered within the small domain near Kiruna (Fig. 2).

Figure 7a shows the 3DVOM +12-h forecast of mountain wave temperature perturbations $T'(x, y, z)$ at $z = 24$ km over northern Scandinavia, valid for 1200 UTC on 25 January 2000. The model predicted a wave field with phase lines oriented approximately perpendicular to the flow, and a dominant horizontal wavelength $\lambda_h \approx 15$ km. The maximum peak-to-peak amplitude is 3.85 K ($\hat{T}_{PEAK} \approx 2$ K).

Figure 7b plots a cross section of stratospheric potential temperatures along the transect shown in pink in Fig. 7a, revealing isentropic wave-induced vertical displacements of ~300 m peak to peak at 22 km. On this day, a DLR Falcon flight was planned and executed to profile forecast mountain wave–induced PSCs near Kiruna. OLEX data from a flight segment near Kiruna are plotted in Fig. 7c, and show small-scale wavelike vertical displacement oscillations in the measured aerosol layers, much as forecast by 3DVOM. High-resolution MM5 hindcasts for this day by Dörnbrack et al. (2002) simulated wave breaking at ~26–28 km, some 2 km above the top edge of the PSC layer in Fig. 7c, which led them to associate the "ripples" near the top of the PSC with Kelvin–Helmholtz instabilities generated within the long-λ_h wave that produces the broad PSC layer. This explanation cannot, however, explain the longer-wavelength larger-amplitude vertical displacement oscillations at z ~20–23 km in Fig. 7c, which must be short-wavelength gravity waves similar to those forecast here by 3DVOM and MWFM.

However, peak-to-peak vertical displacements evident in the lidar imagery are somewhat larger than the Boussinesq 3DVOM model's forecast isentropic vertical displacements in Fig. 7b. To investigate this, postmission hindcasts were performed using the anelastic 3DVOM model. Figure 8 plots 24-h forecasts for the following day (26 January at 1200 UTC), showing Boussinesq and anelastic 3DVOM results in the left and right columns, respectively. Stratospheric wave amplitudes are noticeably larger in the anelastic simulation: at $z = 24$ km, maximum and minimum temperature perturbations are 4.4 and −6.1 K, respectively, yielding $\hat{T}_{PEAK} \approx 5$ K compared to 2–3 K for the corresponding Boussinesq run. This increased amplitude is reflected in larger vertical displacements of isentropic surfaces in Fig. 8d. Similar increases were noted for an anelastic simulation of 25 January (not shown). These vertical displacements agree better with those seen in the lidar data on these days (Figs. 7c and 6d; see also Dörnbrack et al. 2002). Horizontal wavelengths in the anelastic model runs are also noticeably longer than in the Boussinesq runs.

To study these differences further, we diagnose vertical propagation characteristics in the Boussinesq model simulations using the Scorer parameter. The generalized three-dimensional form of the Scorer parameter for a mountain wave under the Boussinesq approximation is (Sawyer 1962; Vosper and Worthington 2002)

$$\ell^2(z) = \frac{N^2 K_h^2}{(\mathbf{U}\cdot\mathbf{K}_h)^2} - \frac{1}{(\mathbf{U}\cdot\mathbf{K}_h)^2}\frac{\mathrm{d}^2}{\mathrm{d}z^2}(\mathbf{U}\cdot\mathbf{K}_h), \qquad (7)$$

where $\mathbf{U}(z)$ is the background horizontal wind vector

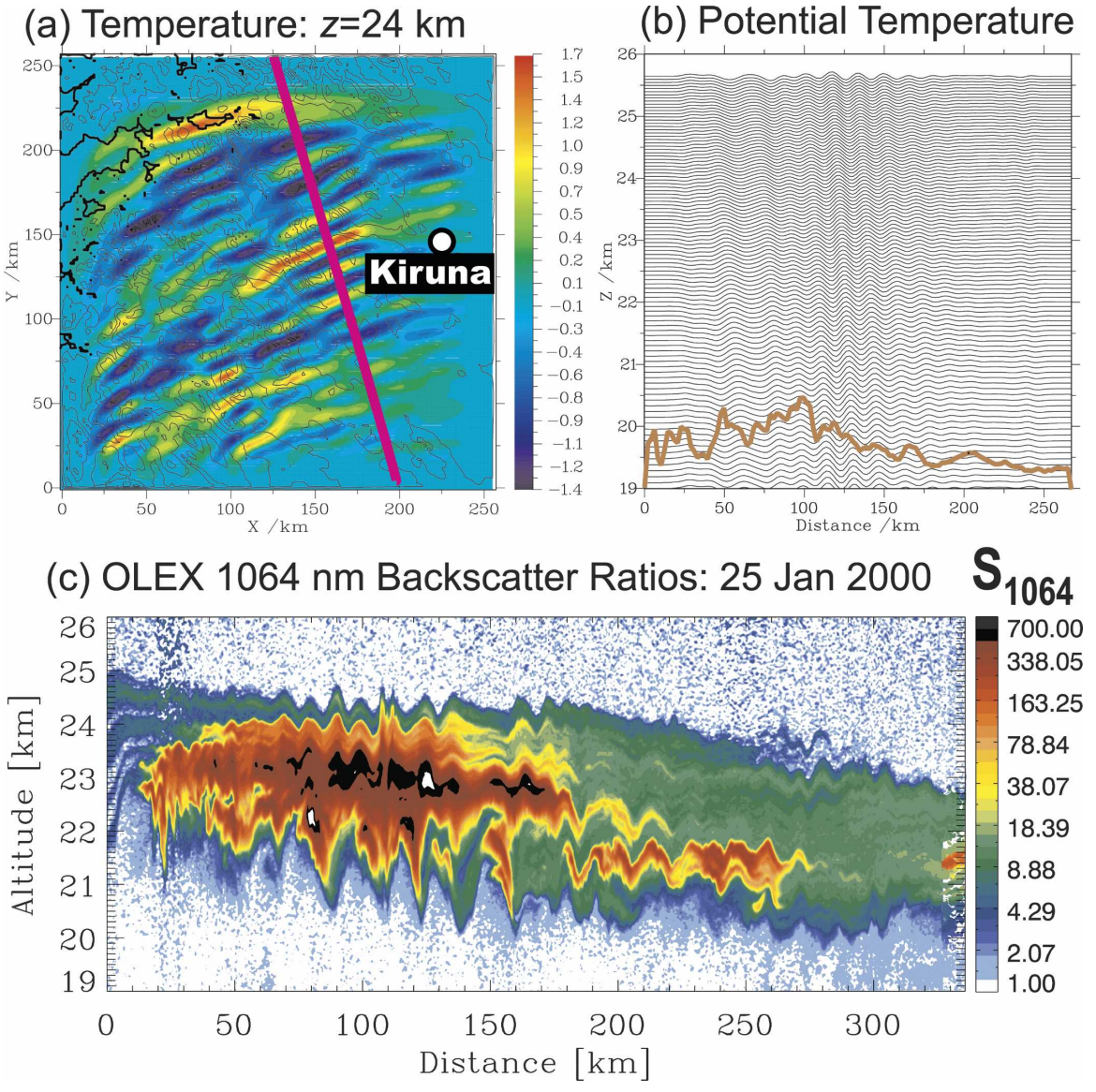

FIG. 7. (a) Forecast 3DVOM temperature perturbations (K; see color bar) at 24 km above sea level for 1200 UTC on 25 Jan 2000. Terrain height contours (solid lines) are also shown at an interval of 500 m; coastline is the boldface line. The pink line shows a horizontal transect, along which stratospheric potential temperatures are profiled vertically and from north to south in (b). Contour interval is 2 K. Underlying topography is plotted in brown. (c) ABRs S_{1064} from OLEX measurements from the DLR Falcon on 25 Jan 2000 along a flight segment near Kiruna (after Dörnbrack et al. 2002).

and $\mathbf{K}_h = (k, l)$ is the horizontal wavenumber vector, such that $\lambda_h = 2\pi/|\mathbf{K}_h|$. Waves with small enough $K_h = |\mathbf{K}_h|$ values (long λ_h) that $\ell^2(z) - K_h^2$ remains positive throughout the troposphere are able to propagate freely into the stratosphere. For shorter-λ_h waves, $\ell^2(z) - K_h^2$ may change sign with altitude, signifying alternating free propagation [$\ell^2(z) - K_h^2 > 0$] and vertical evanescence [$\ell^2(z) - K_h^2 < 0$]. The altitude z_t where $\ell^2(z_t) - K_h^2 = 0$ is a turning point where the wave reflects vertically, leading to a trapped wave if the surface layer is also reflective.

Forecast wind profiles and associated $\ell^2(z)$ profiles for 1200 UTC 25 January are plotted in Figs. 9a and 9b, respectively. There is a marked reduction in $\ell^2(z)$ in the mid- to upper troposphere, indicating vertical evanescence [$\ell^2(z) - K_h^2 < 0$] for short-λ_h waves in this region that will trap these waves in the lower troposphere. Figure 9c plots temperature perturbations from the Boussinesq model cross section in Fig. 7b, from the ground to 30 km. We note strong trapping of wave energy in the troposphere, consistent with the $\ell^2(z)$ profile. Absolute temperature perturbation amplitudes

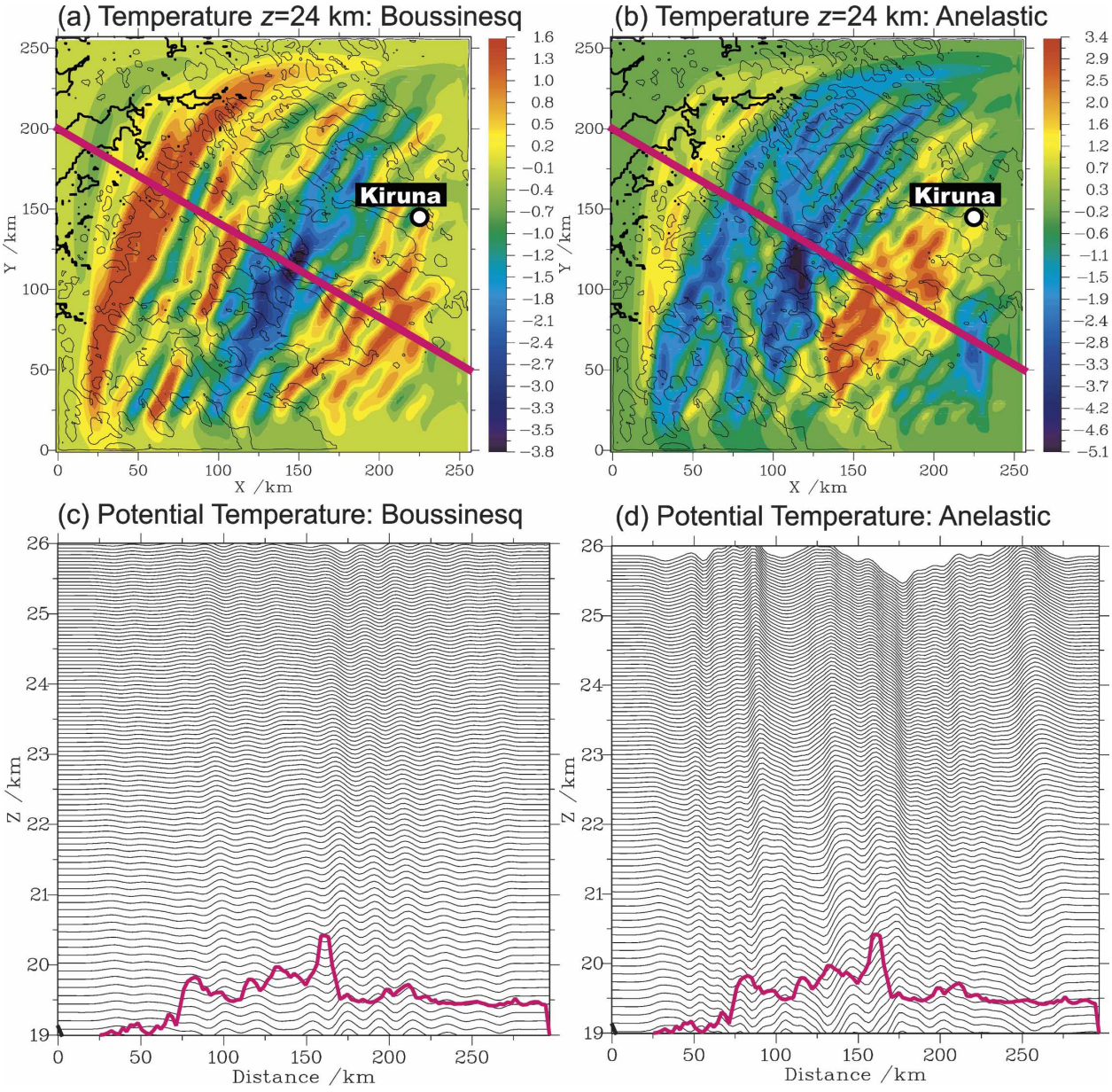

FIG. 8. Forecast temperature perturbations (K; see color bar) at 24 km above sea level for 1200 UTC on 26 Jan 2000 for the (a) Boussinesq and (b) anelastic 3DVOM simulations. Terrain height contours (solid lines) are also shown at an interval of 500 m; coastline is the boldface solid curve. Pink lines show a horizontal transect along which the stratospheric potential temperatures are profiled vertically and from north to south for the (c) Boussinesq and (d) anelastic simulations. Contour interval is 2 K. Underlying topography is plotted as the solid pink curve.

$|T'|$ are as high as 9 K below 5 km, but decay rapidly above 5 km. The trapping is only partial, however, and a small amount of wave energy is able to "tunnel" through the evanescent layer into the lower stratosphere where $\ell^2(z) - K_h^2 > 0$ again.

Thus, tropospheric trapping of wave energy had a major effect on the stratospheric wave fields forecast by 3DVOM over Kiruna. The differences in horizontal wavelengths of stratospheric waves forecast in the anelastic solutions are also presumably caused by sensitivity of the wave solution to changes in the expression for the Scorer parameter compared to the simplified Boussinesq expression (7) (Nance 1997). The importance of vertical reflections to these 3DVOM stratospheric forecasts confirmed the perceived importance of including vertical reflections in the MWFM-2

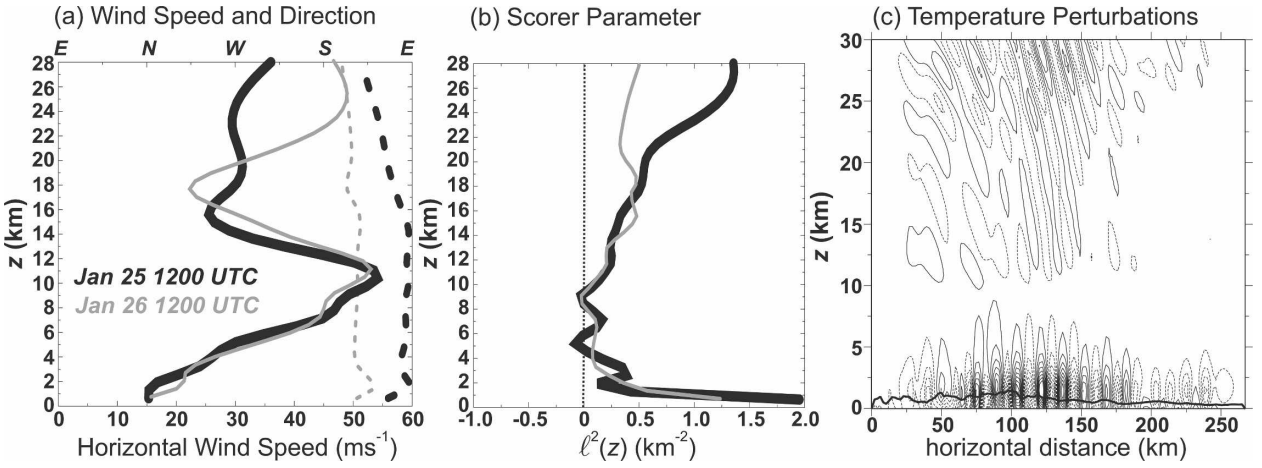

FIG. 9. (a) Profiles of horizontal wind speed (solid) and vector direction (dashed) from 24-h ECMWF forecast data for 25 Jan at 1200 UTC (black) and 26 Jan at 1200 UTC (gray) at 68°N, 18°E. Corresponding Scorer parameters $\ell^2(z)$ are plotted in (b) for a mountain wave horizontal wavevector $\mathbf{K}_h$ directed at 315°. (c) Forecast 3DVOM temperature perturbations (contour interval 1 K) along the transect in Fig. 7a. Solid and dashed contours denote positive and negative values, respectively. Underlying topography is also plotted.

forecast algorithms used during SOLVE/THESEO 2000 (see section 2c).

c. 23 January 2000: PSCs over eastern Greenland

The previous two forecasting examples concentrated on mountain wave PSCs over Scandinavia that were relatively short flight distances from Kiruna. However, the NASA DC-8 can fly continuously for up to 10 h, permitting a large area of potential airborne operations shown in Fig. 1. This area encompassed possible overflights of mountainous Arctic terrain away from Scandinavia, such as Iceland, Greenland, and Svalbard. In addition, permission was granted in some cases for flights into Russian airspace, bringing mountains over Novaya Zemlya, Severnaya Zemlya, Franz Josef Land, and the Urals into play as well (see section 4e). Wider-area MWFM-2 forecasts provided the only forecast guidance on mountain wave PSCs away from Scandinavia and Spitzbergen.

Figure 10 shows a +12-h MWFM-2 forecast of peak mountain wave temperature amplitudes at 30 hPa over an extended geographical region of the Arctic to the west of Kiruna, valid for 23 January 2000 at 1200 UTC. Unlike the previous examples, on this day there was no significant mountain wave activity predicted over Scandinavia. However, large-amplitude stratospheric mountain waves were predicted over the southern and central coasts of Greenland. Indeed, MWFM-2 had been recurrently forecasting large-amplitude waves along the east coast of Greenland for a number of days before this.

Coupled with the cold 30-hPa synoptic temperatures T also predicted here on this day, this forecast predicted mountain wave–induced type II PSCs forming along the eastern coast of central Greenland (i.e., $T - \hat{T}_{\mathrm{PEAK}} < T_{\mathrm{ICE}}$), which was of considerable scientific interest. Studies of PSCs in previous Arctic winters had sug-

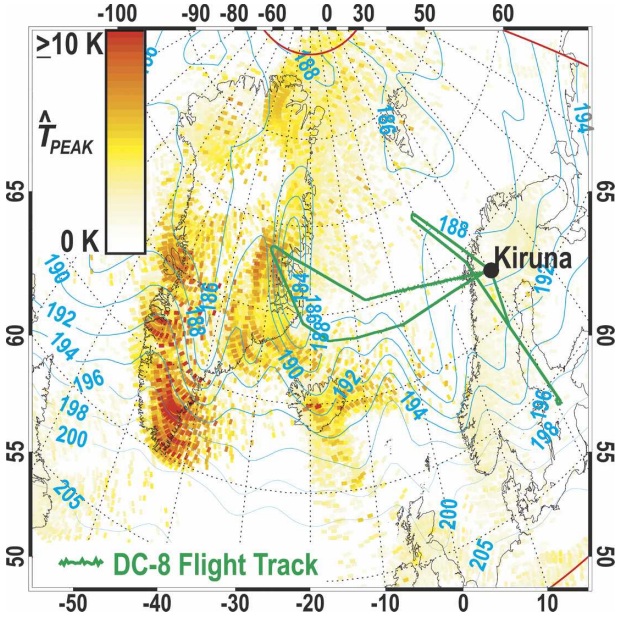

FIG. 10. MWFM-2 +12-h $\hat{T}_{\mathrm{PEAK}}$ forecasts at 30 hPa, valid for 23 January 2000 at 1200 UTC, based on the +12-h operational NOGAPS forecasts from FNMOC. Blue contours show NOGAPS 30-hPa forecast temperatures, and red-yellow pixels show peak mountain wave temperature amplitudes of ray groups, (K) as in Fig. 3a. Color bar scale is linear. DC-8 flight track executed on this day is plotted in green.

gested, with the aid of MWFM hindcasts, that type II PSCs formed recurrently within mountain waves generated by flow across the east coast of Greenland (e.g., Carslaw et al. 1998a). Furthermore, microphysical trajectory calculations suggested that these eastern Greenland wave-induced ice PSCs produced a surviving wake of solid type I PSC particles nucleated on ice that could be transported long distances downstream, possibly to regions in and around Kiruna (Carslaw et al. 1999; Tsias et al. 1999). Yet no direct experimental verification existed for either stratospheric mountain waves over eastern Greenland, or for PSC particles forming within and surviving downstream of these predicted waves. Thus, a segment of the DC-8 flight for this day was planned to fly beneath and then downstream of these forecast mountain wave ice PSCs. The complete flight track flown on 23 January 2000 is plotted in green in Fig. 10.

Figure 11a focuses on the DC-8 flight segment across the east coast of Greenland and then downstream, from 1500 to 1630 UTC. Figure 11b plots S_{1064} from the LaRC lidar during this flight period. On either side of the western apex point of the flight at ~1535 UTC, the lidar measured thick layers of enhanced ABR (S_{1064} ~100–500), indicating the presence of type II PSCs (see also Hu et al. 2002; Svendsen et al. 2005). This thick type II PSC layer slopes upward with increasing time along the westward-heading flight segment (1510–1530 UTC), then slopes back downward with time after the plane has reversed course to eastward (1540–1600 UTC). This sloping PSC structure is consistent with ice forming in the coldest temperature phases of a long-wavelength mountain wave propagating westward with respect to the eastward background winds: see, for example, the earlier mountain wave PSC example in Fig. 6d. Smaller-scale wave structure is also visible in Fig. 11b.

Figure 11c shows the MWFM-2 +12-h forecasts of mountain wave peak temperature amplitudes at 30 hPa from Fig. 10, computed along the DC-8 flight track. The solid curves show mean values, computed by averaging all rays located within 0.25° latitude and 0.5° longitude of the current flight position. The dotted curves show the corresponding maximum $\hat{T}_{\mathrm{PEAK}}$ value of all the rays within this interval. The gray curves show results using both of the ridge databases in Fig. 1, while black curves use only the narrow-ridge database. All forecast curves show enhanced mountain wave amplitudes from 1520 to 1550 UTC, times which correspond to the measurement of sloping type II PSC layers in Fig. 11b. Figure 11d repeats the average peak amplitude calculations for narrow-ridge runs for forecast times ranging from 12 to 60 h, showing that enhanced wave amplitudes along this flight segment were a robust MWFM prediction out to 2.5 days before the flight.

Thus, our forecasts are consistent with the type II mountain wave PSC layer that was observed from the DC-8 in Fig. 11b. These forecast-guided DC-8 observations provided the first direct observational validation that stratospheric mountain waves form over eastern Greenland and produce type II PSCs. Moreover, we see a similarly thick layer of enhanced but lower ABRs in Fig. 11b downstream of the Greenland coast (1600–1630 UTC). In fact, this layer was observed in the lidar data almost all the way back to Kiruna (~1730 UTC). Hu et al. (2002) studied this downstream S_{1064} layer and identified it as a surviving wake of solid NAT particles emanating from the upstream mountain wave PSCs.

d. 14 January 2000: PSCs over northern Greenland

In the three previous cases, mountain wave PSCs were predicted by the models and observed from the DC-8 and Falcon. We now consider two other flights in which mountain wave PSCs were not predicted, but were reported in the DC-8 lidar data by Hu et al. (2002).

On 14 January 2000, both the DC-8 and ER-2 conducted ferry flights to Kiruna from DFRC in California and Westover Air Force Base (AFB) in Massachussetts, respectively, to commence phase 2 of SOLVE/THESEO 2000. To support these flights, MWFM $\hat{T}_{\mathrm{PEAK}}$ forecasts were issued over a very broad area of the Arctic encompassing North America. In Fig. 12 we focus on a smaller region encompassing Greenland and Scandinavia, showing MWFM-2 forecasts of peak mountain wave vertical velocities $\hat{W}_{\mathrm{PEAK}}$ at 50 hPa, rather than $\hat{T}_{\mathrm{PEAK}}$ values at 30 hPa, for reasons that will become clear shortly.

The DC-8 flight track across northern Greenland in Fig. 12 intercepted very little forecast stratospheric mountain wave activity. This led MWFM-2 to predict no mountain wave PSCs along this flight segment. However, as the DC-8 crossed the east coast of Greenland, LaRC lidar data (not shown) recorded $S_{1064} \gtrsim 100$ and strong depolarization at ~22–24 km (Hu et al. 2002; Luo et al. 2003), which implies the presence of an ice PSC. Since synoptic temperatures were too warm for ice PSCs to exist, Hu et al. (2002) and Luo et al. (2003) identified this cloud as a mountain wave–induced ice PSC. If their intepretation is correct, then the MWFM-2 null PSC prediction in Fig. 12 would imply failure of the forecast guidance in this case.

However, recent work has revealed a nonorographic origin for this PSC that is consistent with the original forecast guidance. A high-resolution mesoscale model simulation by Buss et al. (2004) found that this ice PSC

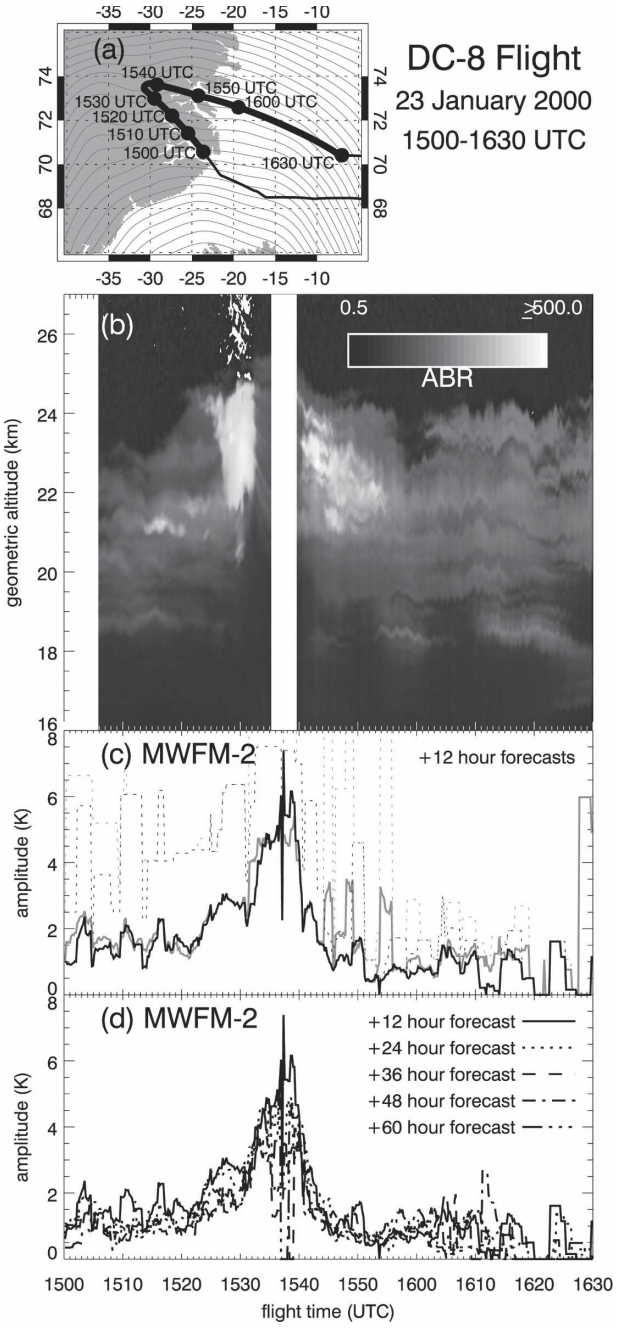

FIG. 11. (a) DC-8 flight segment to and from Greenland on 23 Jan 2000. Gray contours are 1200 UTC 700-hPa geopotential heights from the NOGAPS +12-h forecast, showing eastward flow across topography beneath the flight path. (b) The 1064-nm ABRs, S_{1064}, acquired by the LaRC aerosol lidar on the DC-8 from 1500 to 1630 UTC. White strip omits data where DC-8 roll angles exceeded 5° during the sharp right turn in (a), which tilted the lidar beam off zenith. Shading scale is logarithmic. (c) Mean square (solid) and maximum (dotted) values of the peak MWFM-2 ray temperature amplitudes $\hat{T}_{\mathrm{PEAK}}$ at 30 hPa within ±0.25° latitude and ±0.5° longitude of the flight track, from the +12-h NOGAPS-initialized MWFM-2 forecasts valid at 1200 UTC. Solid curves are results using only the narrow ridges in Fig. 1b, while gray curves show results using all the ridges in Fig. 1. (c) Collated MWFM-2 results using narrow-ridge database based on NOGAPS 12-, 24-, 36-, 48-, and 60-h forecasts for 23 Jan at 1200 UTC.

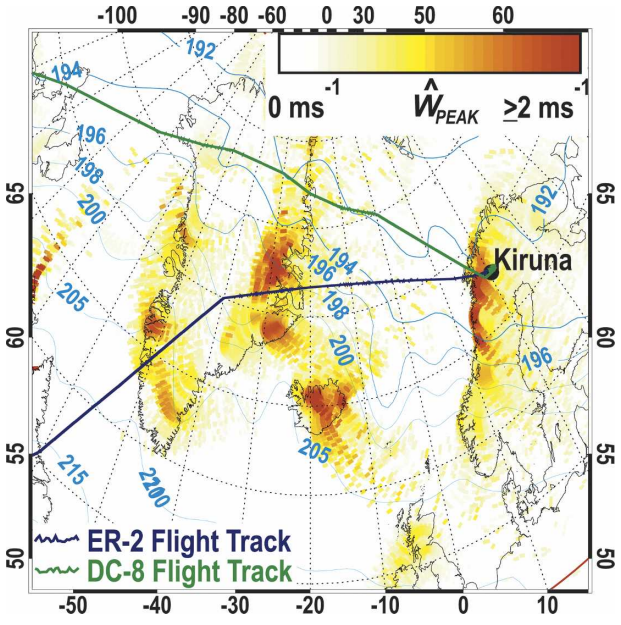

FIG. 12. MWFM-2 +24-h forecasts of peak mountain wave vertical velocity amplitudes, $\hat{W}_{PEAK}$, at 50 hPa (near ER-2 cruise altitude), valid for 14 Jan 2000 at 1200 UTC, based on the +24-h operational NOGAPS forecasts from FNMOC. Blue contours show NOGAPS 50-hPa forecast temperatures (K), and red-yellow pixels show peak mountain wave vertical velocity amplitudes of ray groups. Color bar scale is linear. The DC-8 and ER-2 flight tracks executed on this day are plotted in green and dark blue, respectively.

was produced by a stratospheric gravity wave produced by either spontaneous adjustment emission from or unstable vertical shear in the tropospheric jet stream. Their model simulations also revealed little if any collocated mountain wave activity along this DC-8 flight segment across Greenland, since simulations using reduced Greenland topography produced very similar-looking stratospheric gravity wave fields. These findings, then, are in fact consistent with the original MWFM-2 forecast in Fig. 12.

The mesoscale model runs of Buss et al. (2004) did, however, find evidence of stratospheric mountain waves intercepting the ER-2 flight track on the east coast of central Greenland, and little evidence of jet-generated gravity waves there. This too appears to be consistent with the MWFM-2 forecast in Fig. 12, which shows significant mountain wave amplitudes at this portion of the ER-2 flight, with $\hat{W}_{\mathrm{PEAK}} \approx 1.5$–$2\ \mathrm{m\ s^{-1}}$ at 50 hPa, the approximate cruise altitude of the ER-2 at this time.

To study this more quantiatively, Fig. 13a focuses on the ER-2 flight segment from 1630 to 1815 UTC. Figure 13b plots potential temperatures derived from the ER-2 MTP instrument several kilometers above and below

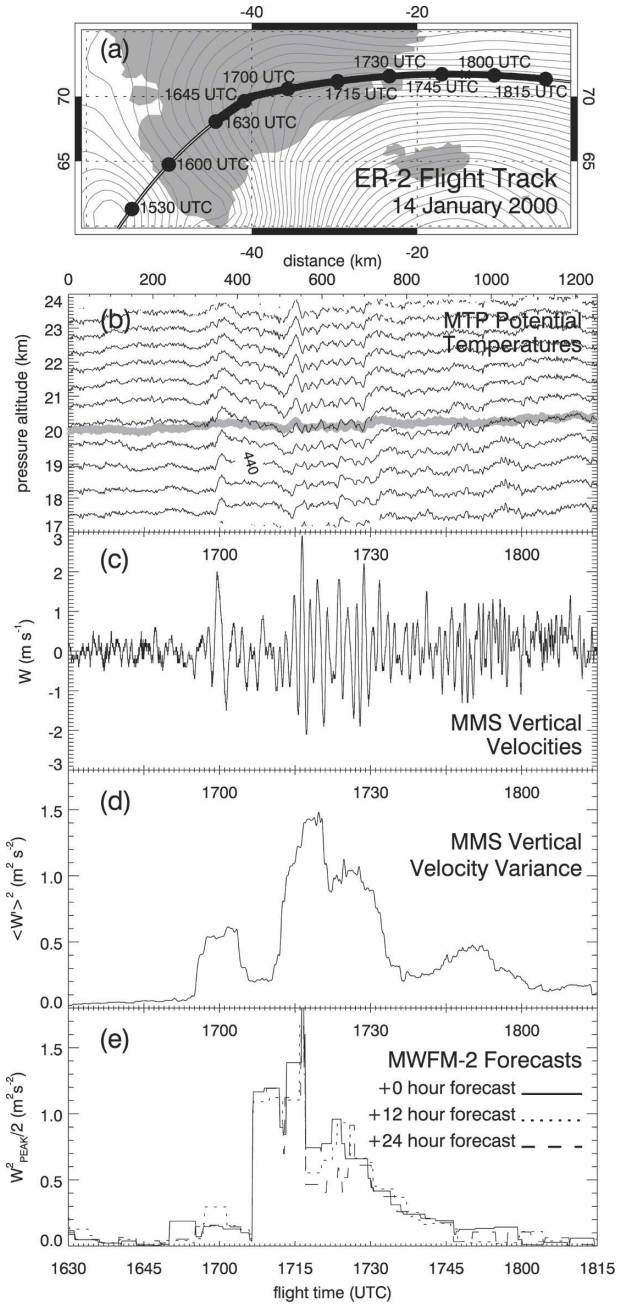

FIG. 13. (a) The ER-2 flight segment across Greenland on 14 Jan 2000. Gray contours are 1800 UTC 700-hPa geopotential heights from the NOGAPS +18-h forecast. (b) Potential temperature surfaces derived from MTP temperature profiles along the ER-2 flight track from 1630 to 1815 UTC. Contours are spaced every 10 K with the 440-K contour labeled. Gray curve shows pressure altitude of ER-2 derived from the MMS. (c) Vertical velocities W measured in situ from ER-2 by the MMS. (d) Vertical velocity variance computed using a running average with a window width of 50 km along track (~8 min flight time). (e) Maximum MWFM-2 ray vertical velocity variances $\hat{W}^2_{\mathrm{PEAK}}/2$ at 50 hPa within ±0.5° latitude and ±1.0° longitude of the ER-2 flight track, corresponding roughly to the width of the averaging window in (d). Results derived from the 0-, +12-, and +24-h NOGAPS-initialized forecasts valid at 1200 UTC are plotted with solid, dotted, and dashed curves, respectively.

the flight altitude (shown in gray), while Fig. 13c plots MMS vertical velocities $W(t)$ measured at flight altitude. Figure 13d computes the MMS vertical velocity variance using a 50-km along-track sliding window. MTP and MMS data both show enhanced small-scale fluctuations at ~1710–1735 UTC, and some smaller-amplitude activity immediately before and after this period. There is little or no fluctuating activity from 1630 to 1655 UTC.

Figure 13e shows the variance $\hat{W}^2_{\mathrm{PEAK}}/2$ of the largest-amplitude MWFM-2 ray in the +12 h forecast located within 0.5° latitude and 1° longitude of the ER-2 flight track, which corresponds roughly to the 50-km averaging window used in Fig. 13d. We see enhanced MWFM-2 ray variance along the flight track from ~1710 to 1730 UTC with maximum values ~1.5 $\mathrm{m^2\,s^{-2}}$, very similar to what is seen in the MMS variances in Fig. 13d. Furthermore, MWFM-2 predicted little or no wave activity from 1600 to 1650 UTC, as observed, despite the fact that this flight segment occurs over elevated surface terrain. There is also evidence of weaker wave activity downstream of Greenland from 1730 to 1800 UTC.

Thus, the ER-2 data validate the salient features of the MWFM-2 forecast along the ER-2 flight track on this day. We note in conclusion that, unlike the "straight shot" flight path of the DC-8 to Kiruna, the ER-2 flight track in Fig. 12 was diverted to the north. This flight path was chosen based on the two regions over southern and southeastern Greenland where MWFM-2 predicted enhanced wave amplitudes in Fig. 12. These wave fields were forecast by MWFM to produce turbulence at 50–70 hPa and lay on the straight-shot ER-2 flight track from Westover AFB to Kiruna. The diverted flight path was allowed to pass through the more northern mountain wave fields predicted by MWFM-2 in Figs. 12 and 13 because these waves were predicted to be nonturbulent. The ER-2 pilot reported light-to-absent turbulence throughout this flight.

e. 10 December 1999: PSCs near Franz Josef Land

Franz Josef Land is an archipelago of over 100 small ice-covered islands in the high Arctic (~81°N, 45–65°E). A DC-8 flight segment in and around Franz Josef Land on 10 December 1999 recorded moderately enhanced ABRs (S_{1064} ~10) and high depolarization, indicative of solid type Ia NAT PSC particles (Hu et al. 2002; Pagan et al. 2004). These flights were designed to sample regions where forecast synoptic stratospheric temperatures were cold enough to support NAT. However, since the ABRs were confined in and around Franz Josef Land and showed structure, Hu et al. (2002) tentatively associated these solid NAT PSCs

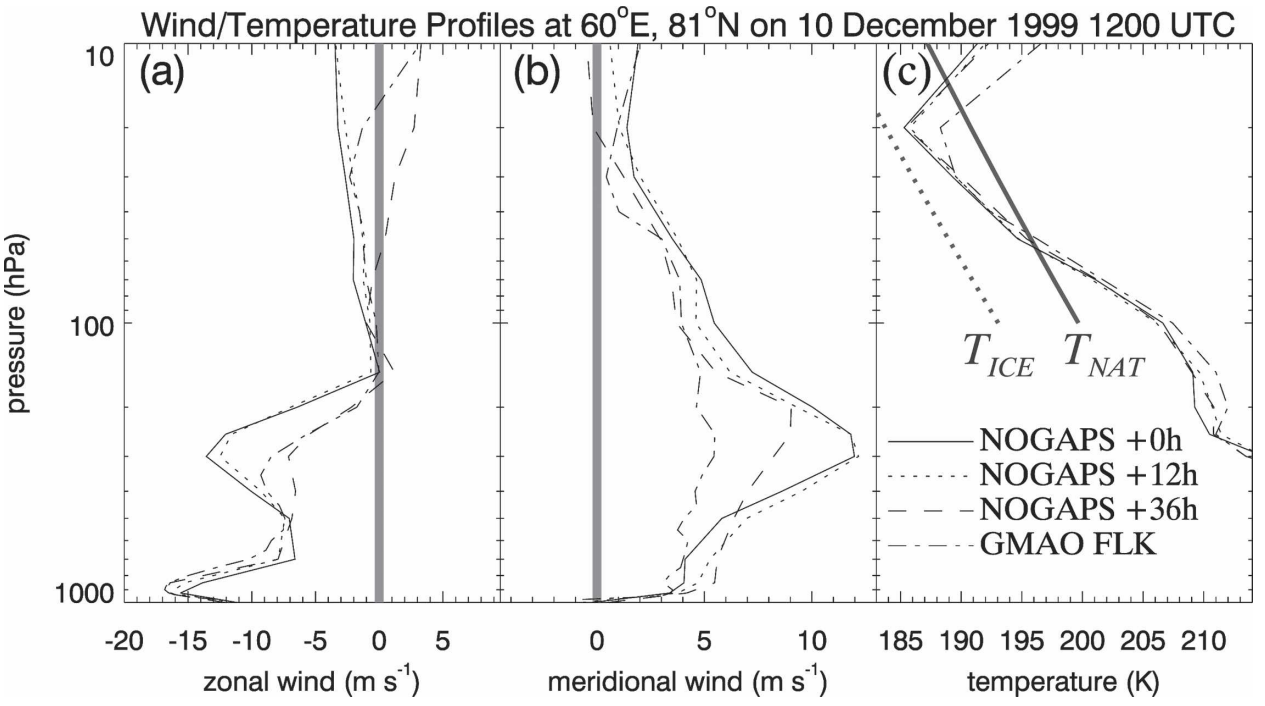

FIG. 14. Profiles of (a) zonal wind, (b) meridional wind, and (c) temperature over Franz Josef Land (81°N, 60°E) at 1200 UTC 10 Dec 1999 from the NOGAPS analysis, +12-h and +36-h forecasts, and GMAO FLK analysis (see Table 2). Gray curves in (c) show T_{NAT} and T_{ICE} assuming 5 ppmv of H_2O and 10 ppbv of HNO_3 (Hanson and Mauersberger 1988; Marti and Mauersberger 1993).

with mountain waves radiated from Franz Josef Land, with NAT possibly forming on ice produced by mountain wave cooling nearby.

MWFM-2 forecasts predicted essentially no stratospheric mountain wave activity over Franz Josef Land at this time because stratospheric winds were extremely weak (see Fig. 14), presenting critical levels to most mountain waves propagating upward from below. Thus, the MWFM-2 forecasts and postanalyses argue that local mountain wave activity played no role in producing these solid NAT particles, supporting similar conclusions of Hitchman et al. (2003) and Pagan et al. (2004). While Hitchman et al. (2003) found evidence for jet-generated gravity waves organizing type I PSC structures observed in DC-8 lidar data near Novaya Zemlya and Severnaya Zemlya on 7 and 12 December, Pagan et al. (2004) argued that the amplitudes of these waves were too weak to form ice as nucleation sites for NAT. So, while local synoptic temperatures are cold enough to maintain these NAT particles (see Fig. 14c), their nucleation origins remain unclear (Pagan et al. 2004).

5. Summary and conclusions

We have assessed an initial coordinated effort to provide operational multimodel forecasts of mountain wave PSCs for planning scientific measurement flights of instrumented aircraft during the SOLVE/THESEO 2000 campaign in the Arctic winter of 1999/2000. Our observational record of choice for validating these forecasts was lidar aerosol backscatter ratios at 1064 nm, S_{1064}, acquired from the NASA DC-8. On five of these flights, PSCs were observed that appeared to be mountain wave related (Hu et al. 2002). We have compared the forecast guidance with available measurements from the DC-8 and other sources.

The extended wave-induced type I–II PSC event of 25–27 January 2000 was an ideal case for these forecasting models, since it occurred over northern Scandinavia where all three models were issuing forecasts. The models accurately predicted the timing and locations of these mountain wave PSCs up to 3 days in advance. We have shown how the acquired PSC data agreed very closely with the models' predicted PSC locations. These forecasts allowed aircraft and balloons to measure mountain wave–induced PSCs in unprecedented detail (Voigt et al. 2000; Dörnbrack et al. 2002; Hu et al. 2002). These data have since motivated detailed microphysical trajectory modeling studies that have improved our understanding of microphysics and chemical processing of air passing through mountain wave PSCs (Fueglistaler et al. 2003; Svendsen et al. 2005).

Another mountain wave–induced type II PSC was predicted over eastern Greenland on 23 January 2000 in a region where only the MWFM was issuing forecasts. On the DC-8 flight that profiled this predicted mountain wave PSC, onboard lidars measured tilted layers of high S_{1064} in the stratosphere over eastern Greenland, indicating type II PSCs forming in the cool phases of a mountain wave. Their locations along the flight track correlated closely with regions of enhanced mountain wave temperature amplitudes in the MWFM-2 forecasts. This forecast guidance provided PSC data that verified earlier hypotheses of Carslaw et al. (1999) and Tsias et al. (1999) that Greenland mountain waves can form both type II PSCs within the waves and surviving wakes of solid type Ia PSC particles long distances downstream.

On 30 November 1999, the DC-8 was descending into Kiruna when type II PSCs were observed visually to the south. MWFM-2 forecasts predicted mountain wave–induced ice PSCs forming over southern Scandinavia on this day. Limited available data, based on visual photography and a local radiosonde sounding, all confirm the basic details of the original forecast.

On 14 January 2000, a wavelike PSC was reported in DC-8 lidar data over northeastern Greenland, despite the fact that the MWFM predicted no mountain wave PSCs forming here. Our analysis of this event accords with recent work by Buss et al. (2004), who argued that this PSC was formed by a nonorographic gravity wave radiated from the jet stream, not a mountain wave. We reinforced this conclusion by analyzing MWFM forecasts for the ER-2 flight across the east coast of central Greenland on this same day. Buss et al. (2004) argued that stratospheric mountain waves arose here and intercepted the ER-2 flight track. The MWFM-2 forecasts support this conclusion, and show good agreement with fluctuations in stratospheric MMS and MTP data acquired from the ER-2 along this flight segment.

Finally, on 10 December 1999 type I PSCs were observed in DC-8 lidar data near Franz Josef Land, despite MWFM-2 predicting insignificant mountain wave amplitudes here on this day. Weak stratospheric winds severely suppressed amplitudes of mountain waves that radiated from these islands on this day. Our forecasts support recent conclusions that stratospheric mountain waves from Franz Josef Land played no role in the formation of these clouds (Hitchman et al. 2003; Pagan et al. 2004).

In summary, the PSC data from all five DC-8 flights are consistent with the original forecast guidance. Despite this success, our review has highlighted some areas where future forecasting efforts of this type could be improved.

First, 3DVOM used a linearized set of equations for flow over orography under the Boussinesq approximation, in order to provide computationally fast high-resolution forecasts. Postanalysis of these 3DVOM forecasts revealed systematic underpredictions of wave amplitudes, and better results when anelastic equation sets were used instead. Thus, high-resolution regional orographic flow models of this type should ideally incorporate anelastic rather than Boussinesq formulations for future forecasting efforts.

Second, at least two examples of PSCs measured from the DC-8 during SOLVE/THESEO 2000 were either produced or organized by gravity waves radiated from the jet stream, rather than from mountains (Hitchman et al. 2003; Buss et al. 2004). Nonorographic stratospheric gravity waves were not specifically forecast during SOLVE/THESEO 2000. It is still unclear how common nonorographic gravity wave PSC events are and, thus, how important they are microphysically: some initial diagnostic estimates of jet stream imbalance during the SOLVE/THESEO 2000 winter by Buss et al. (2004) suggest they may be infrequent. Nonetheless, it would be desirable to supplement mountain wave forecasts with forecasts of other nonorographic sources of potentially large-amplitude gravity waves.

These recommendations were integrated into a high-resolution stratospheric forecasting effort for DC-8 flights from Kiruna during the SOLVE-II mission of 2002–03, which was designed to provide the validation data that SOLVE had hoped to provide before the launch of SAGE III was delayed (see, e.g., McCormack et al. 2004). Similar forecasting was also performed in support of NASA's Polar Aura Validation Experiment during January–February 2005. Our assessments here should provide useful guidance for high-resolution forecasting support for future airborne stratospheric science missions, such as the remaining Aura Validation Experiments planned for 2005–07.

Acknowledgments. The second author acknowledges the reliable access to the ECMWF forecast data in the framework of his ECMWF special project. All of us thank the in-field meteorology and flight-planning teams during SOLVE/THESEO 2000 for the open way in which they integrated our new forecasts into overall mission planning. SDE thanks Paul Newman and Leslie Lait of NASA Goddard Space Flight Center for access to GMAO and NCEP fields, and to Tim Hogan and colleagues at NRL's Marine Meteorology Division in Monterey, California, for timely access to operational NOGAPS forecast fields. We also thank Chris Hostetler for his LaRC lidar data that were used in this study. SDE's work was funded by the Office of Naval

Research and NASA's Upper Atmosphere Research Program and Geospace Sciences Program. Work by MJM at the Jet Propulsion Laboratory, California Institute of Technology, was performed under contract with the National Aeronautics and Space Administration.

APPENDIX

MWFM Initialization

a. Froude number initialization

Ideally, we associate the surface flow level z_s with each ridge's base altitude z_b. When $\mathrm{Fr}^{-1} > 1$, we progressively move upward from z_b until we reach a new base altitude $\hat{z}_b = z_b + \Delta h$, where the reduced ridge elevation presented to the flow, $\hat{h} = h - \Delta h$, is such that $\hat{\mathrm{Fr}}^{-1} = N(\hat{z}_b)\hat{h}/|U(\hat{z}_b)| \leq 1$.

However, since complex topography is decomposed into a series of overlaying ridges, as shown in Fig. 1, some ridges have base altitudes z_b that lie some distance below the surface topographic elevation of the nearest grid box of the NWP model supplying meteorological profiles for initialization. In this case, the $|U(z_b)|$ and $N(z_b)$ values needed for the Froude number calculation are subterranean values that are either undefined in the NWP output file or else have been interpolated to this subterranean local level, making the calculation either impossible or highly inaccurate.

To avoid these problems, in the MWFM we use the peak ridge altitude $z_s = z_b + h$ for our Froude number calculation. If $\mathrm{Fr}^{-1} > 1$, we do not change z_s but instead simply clip the peak ridge height to a reduced value $\hat{h} = h\,\mathrm{Fr}$, which yields $\hat{\mathrm{Fr}}^{-1} = 1$ at z_s.

b. Ray initialization

The total number of rays launched from each ridge, $I = I_K I_\varphi$, consists of $i_k = 1, \ldots, I_K$ different horizontal wavenumber harmonics per ridge, each launched at $i_\varphi = 1, \ldots, I_\varphi$ separate horizontal propagation harmonics distributed at equispaced intervals within the sector $\varphi_{\mathrm{OR}} - 90^\circ < \varphi_{i_\varphi} < \varphi_{\mathrm{OR}} + 90^\circ$, where $\varphi_{\mathrm{OR}} = \varphi_{\mathrm{LONG}} \pm 90^\circ$ lies orthogonal to the long axis of the ridge (i.e., parallel to its short axis of length L).

For rapid turnaround of SOLVE/THESEO 2000 forecasts, we chose $I_K = 3$ and $I_\varphi = 18$ or 36, yielding $I = 54$ or 108 rays per ridge with horizontal wavenumbers for each ray i given by

$$(\mathbf{K}_h)_i = i_k\left(\frac{a}{L}\right)(\cos\varphi_{i_\varphi}, \sin\varphi_{i_\varphi}), \qquad \text{(A1)}$$

where $i = (i_k - 1)I_\varphi + i_\varphi$. We chose $a = 2$ based on typical peaks in Fourier integral wave solutions over idealized obstacle shapes (Shutts 1998; Broutman et al. 2001). However, this value varies with obstacle shape and hence is somewhat tunable: later MWFM-2 studies used slightly smaller values of $a = 1.5$ (Hertzog et al. 2002; Jiang et al. 2004).

Largest initial ray amplitudes are assigned to those rays with $(\mathbf{K}_h)_i$ directed parallel to φ_{OR}. Ray amplitudes at other propagation azimuths are scaled down as a function of $|\varphi_{i_\varphi} - \varphi_{\mathrm{OR}}|$. The degree of azimuthal suppression depends on the ridge's "quality" parameter q, a normalized term ($0 \leq q \leq 1$) that defines how well the original topography was represented by the fit with a quasi-2D ridge function: $q \sim 1$ indicates a good fit, suggesting the original topography was quasi-2D and ridge like, whereas $q = 1$ usually indicates a fit to a more symmetric 3D obstacle. Ridges with small q produce rays of comparable amplitude in all azimuth directions φ_i, whereas for $q \sim 1$ rays significantly attenuate in amplitude as a function of increasing $|\varphi_{i_\varphi} - \varphi_{\mathrm{OR}}|$. This allows MWFM-2 to generate 2D plane mountain waves from 2D ridgelike topography (Bacmeister et al. 1994) that have linear phase lines parallel to the long axis of the ridge, as well as 3D diverging "ship-wake" patterns from flow across more symmetric 3D obstacles. For some simple ray examples, see Gjevik and Marthinsen (1978), Shutts (1998), and Broutman et al. (2001).

REFERENCES

Austin, J., and Coauthors, 2003: Uncertainties and assessments of chemistry–climate models of the stratosphere. *Atmos. Chem. Phys.,* **3,** 1–27.

Bacmeister, J. T., P. A. Newman, B. L. Gary, and K. R. Chan, 1994: An algorithm for forecasting mountain wave–related turbulence in the stratosphere. *Wea. Forecasting,* **9,** 241–253.

——, S. D. Eckermann, P. A. Newman, L. Lait, K. R. Chan, M. Loewenstein, M. H. Proffitt, and B. L. Gary, 1996: Stratospheric horizontal wavenumber spectra of winds, potential temperature and atmospheric tracers observed by high-altitude aircraft. *J. Geophys. Res.,* **101,** 9441–9470.

Barker, E., 1992: Design of the navy's multivariate optimum interpolation analysis system. *Wea. Forecasting,* **7,** 220–231.

Becker, G., R. Müller, D. S. McKenna, M. Rex, and K. S. Carslaw, 1998: Ozone loss rates in the Arctic stratosphere in the winter 1991/1992: Model calculations compared with match results. *Geophys. Res. Lett.,* **25,** 4325–4328; Correction, **26,** 327.

Broutman, D., J. W. Rottman, and S. D. Eckermann, 2001: A hybrid method for analyzing wave propagation from a localized source, with application to mountain waves. *Quart. J. Roy. Meteor. Soc.,* **127,** 129–146.

——, ——, and ——, 2003: A simplified Fourier method for nonhydrostatic mountain waves. *J. Atmos. Sci.,* **60,** 2686–2696.

Buss, S., A. Hertzog, C. Hostetler, T. P. Bui, D. Lüthi, and H. Wernli, 2004: Analysis of a jet stream induced gravity wave

associated with an observed stratospheric ice cloud over Greenland. *Atmos. Chem. Phys.,* **4,** 1183–1200.

Caplan, P., and H.-L. Pan, 2000: Changes to the 1999 NCEP operational MRF/AVN global analysis/forecast system. National Weather Service Technical Procedures Bull. 452, 15 pp. [Available online at http://www.nws.noaa.gov/om/tpb/indexb.htm.]

Cariolle, D., S. Müller, F. Cayla, and M. P. McCormick, 1989: Mountain waves, polar stratospheric clouds, and the ozone depletion over Antarctica. *J. Geophys. Res.,* **94,** 11 233–11 240.

Carslaw, K. S., and Coauthors, 1998a: Increased stratospheric ozone depletion due to mountain-induced atmospheric waves. *Nature,* **391,** 675–678.

——, and ——, 1998b: Particle microphysics and chemistry in remotely observed mountain polar stratospheric clouds. *J. Geophys. Res.,* **103,** 5785–5796.

——, T. Peter, J. T. Bacmeister, and S. D. Eckermann, 1999: Widespread solid particle formation by mountain waves in the Arctic stratosphere. *J. Geophys. Res.,* **104,** 1827–1836.

Chipperfield, M. P., and R. L. Jones, 1999: Relative influences of atmospheric chemistry and transport on Arctic ozone levels. *Nature,* **400,** 551–554.

Davies, L. A., and A. R. Brown, 2001: Assessment of which scales of orography can be credibly resolved in a numerical model. *Quart. J. Roy. Meteor. Soc.,* **127,** 1225–1237.

Dee, D. P., and R. Todling, 2000: Data assimilation in the presence of forecast bias: The GEOS moisture analysis. *Mon. Wea. Rev.,* **128,** 3269–3282.

Denning, R. F., S. L. Guidero, G. S. Parks, and B. L. Gary, 1989: Instrument description of the airborne Microwave Temperature Profiler. *J. Geophys. Res.,* **94,** 16 757–16 765.

Derber, J., and Coauthors, 1998: Changes to the 1998 NCEP operational MRF model analysis/forecast system. National Weather Service Technical Procedures Bull. 449, 37 pp. [Available online at http://www.nws.noaa.gov/om/tpb/indexb.htm.]

Dörnbrack, A., M. Leutbecher, H. Volkert, and M. Wirth, 1998: Mesoscale forecasts of stratospheric mountain waves. *Meteor. Appl.,* **5,** 117–126.

——, T. Birner, A. Fix, H. Flentje, A. Meister, H. Schmid, E. V. Browell, and M. J. Mahoney, 2002: Evidence for inertia gravity waves forming polar stratospheric clouds over Scandinavia. *J. Geophys. Res.,* **107,** 8287, doi:10.1029/2001JD000452.

Dudhia, J., 1993: A nonhydrostatic version of the Penn State–NCAR Mesoscale Model: Validation tests and simulation of an Atlantic cyclone and cold front. *Mon. Wea. Rev.,* **121,** 1493–1513.

Dutton, J. A., and G. H. Fichtl, 1969: Approximate equations of motion for liquids and gases. *J. Atmos. Sci.,* **26,** 241–254.

Eckermann, S. D., 2002: Climatology of mountain wave-induced turbulence in the stratosphere over Central Asia: October–December 1994–2001. Naval Research Laboratory Tech. Memo. NRL/MR/7640-02-8594, 52 pp.

——, and P. Preusse, 1999: Global measurements of stratospheric mountain waves from space. *Science,* **286,** 1534–1537.

——, D. Broutman, and J. T. Bacmeister, 2000: Aircraft encounters with mountain wave-induced clear air turbulence: Hindcasts and operational forecasts using an improved global model. Preprint*, Ninth Conf. on Aviation, Range, and Aerospace Meteorology,* Orlando, FL, Amer. Meteor. Soc., 456–459.

——, J. Ma, and D. Broutman, 2004: The NRL Mountain Wave Forecast Model (MWFM). Preprints, *Symp. on the 50th Anniversary of Operational Numerical Weather Prediction,* University of Maryland, College Park, MD, Amer. Meteor. Soc., P2.9. [Available online at http://uap-www.nrl.navy.mil/dynamics/papers/Eckermann_P2.9-reprint.pdf.]

Edouard, S., B. Legras, F. Lefévre, and R. Eymard, 1996: The effect of small-scale inhomogeneities on ozone depletion in the Arctic. *Nature,* **384,** 444–447.

Flentje, H., W. Renger, M. Wirth, and W. A. Lahoz, 2000: Validation of contour advection simulations with airborne lidar measurements of filaments during the Second European Stratospheric Arctic and Midlatitude Experiment (SESAME). *J. Geophys. Res.,* **105,** 15 417–15 437.

Fritts, D. C., and P. K. Rastogi, 1985: Convective and dynamical instabilities due to gravity wave motions in the lower and middle atmosphere. *Radio Sci.,* **20,** 1247–1277.

Fueglistaler, S., and Coauthors, 2003: Detailed modeling of mountain wave PSCs. *Atmos. Chem. Phys.,* **3,** 697–712.

Gjevik, B., and T. Marthinsen, 1978: Three-dimensional lee-wave pattern. *Quart. J. Roy. Meteor. Soc.,* **104,** 947–957.

Grell, G. A., J. Dudhia, and D. R. Stauffer, 1994: A description of the fifth-generation Penn State/NCAR mesoscale model (MM5). NCAR Note 398, 121 pp.

Hanson, D., and K. Mauersberger, 1988: Laboratory studies of the nitric acid trihydrate: Implications for the South Pole stratosphere. *Geophys. Res. Lett.,* **15,** 855–858.

Hertzog, A., F. Vial, A. Dörnbrack, S. D. Eckermann, B. M. Knudsen, and J.-P. Pommereau, 2002: In-situ observations of gravity waves and comparisons with numerical simulations during the SOLVE/THESEO 2000 campaign. *J. Geophys. Res.,* **107,** 8292, doi:10.1029/2001JD001025.

Hitchman, M. H., M. L. Buker, G. J. Tripoli, E. V. Browell, W. B. Grant, C. Hostetler, T. J. McGee, and J. F. Burris, 2003: Nonorographic generation of Arctic polar stratospheric clouds during December 1999. *J. Geophys. Res.,* **108,** 8325, doi:10.1029/2001JD001034.

Hogan, T. F., and T. Rosmond, 1991: The description of the Navy Operational Global Atmospheric Prediction System's spectral forecast model. *Mon. Wea. Rev.,* **119,** 1786–1815.

Hood, L. L., B. E. Soukharev, M. Fromm, and J. P. McCormack, 2001: Origin of extreme ozone minima at middle to high northern latitudes. *J. Geophys. Res.,* **106,** 20 925–20 940.

Hu, R.-M., and Coauthors, 2002: Microphysical properties of wave polar stratospheric clouds retrieved from lidar measurements during SOLVE/THESEO 2000. *J. Geophys. Res.,* **107,** 8294, doi:10.1029/2001JD001125.

Jacob, D. J., and Coauthors, 2003: Transport and Chemical Evolution over the Pacific (TRACE-P) aircraft mission: Design, execution, and first results. *J. Geophys. Res.,* **108,** 9000, doi:10.1029/2002JD003276.

Jakob, C., and Coauthors, 2000: The IFS cycle CY21r4 made operational in October 1999. *ECMWF Newsletter,* Vol. 87, European Centre for Medium-Range Weather Forecasts, Reading, United Kingdom, 2–9. [Available online at http://www.ecmwf.int/publications/newsletters/list.html.]

Jiang, J. H., S. D. Eckermann, D. L. Wu, and J. Ma, 2004: A search for mountain waves in MLS stratospheric limb radiances from the winter Northern Hemisphere: Data analysis and global mountain wave modeling. *J. Geophys. Res.,* **109,** D03107, doi:10.1029/2003JD003974.

Kanamitsu, M., 1988: Description of the NMC Global Data Assimilation and Forecast System. *Wea. Forecasting,* **4,** 335–342.

Knudsen, B. M., J.-P. Pommereau, A. Garnier, M. Nunes-Pinharanda, L. Denis, P. Newman, G. Letrenne, and M. Durand, 2002: Accuracy of analyzed stratospheric temperatures in the winter Arctic vortex from infrared Montgolfier long-duration balloon flights, 2, Results. *J. Geophys. Res.,* **107,** 4316, doi:10.1029/2001JD001329.

Lahoz, W. A., 1999: Predictive skill of the UKMO Unified Model in the lower stratosphere. *Quart. J. Roy. Meteor. Soc.,* **125,** 2205–2238.

Lander, J., and B. J. Hoskins, 1997: Believable scales and parameterizations in a spectral transform model. *Mon. Wea. Rev.,* **125,** 292–303.

Lane, T. P., M. J. Reeder, B. R. Morton, and T. L. Clark, 2000: Observations and numerical modeling of mountain waves over the Southern Alps of New Zealand. *Quart. J. Roy. Meteor. Soc.,* **126,** 2765–2788.

Lee, A. M., G. D. Carver, M. P. Chipperfield, and J. A. Pyle, 1997: Three-dimensional chemical forecasting: A methodology. *J. Geophys. Res.,* **102,** 3905–3919.

Leutbecher, M., and H. Volkert, 2000: The propagation of mountain waves into the stratosphere: Quantitative evaluation of three-dimensional simulations. *J. Atmos. Sci.,* **57,** 3090–3108.

Lipps, F. B., and R. S. Hemler, 1982: A scale analysis of deep moist convection and some related numerical calculations. *J. Atmos. Sci.,* **39,** 2192–2210.

Luo, B. P., C. Voigt, S. Fueglistaler, and T. Peter, 2003: Extreme NAT supersaturations in mountain wave ice PSCs: A clue to NAT formation. *J. Geophys. Res.,* **108,** 4441, doi:10.1029/2002JD003104.

Lutman, E. R., J. A. Pyle, M. P. Chipperfield, D. J. Lary, J. Kilbane-Dawe, J. W. Waters, and N. Larsen, 1997: Three-dimensional studies of the 1991/1992 Northern Hemisphere winter using domain-filling trajectories with chemistry. *J. Geophys. Res.,* **102,** 1479–1488.

Manney, G. L., J. L. Sabutis, S. Pawson, M. L. Santee, B. Naujokat, R. Swinbank, M. E. Gelman, and W. Ebisuzaki, 2003: Lower stratospheric temperature differences between meteorological analyses in two cold Arctic winters and their impact on polar processing studies. *J. Geophys. Res.,* **108,** 8328, doi:10.1029/2001JD001149.

Marks, C. J., and S. D. Eckermann, 1995: A three-dimensional nonhydrostatic ray-tracing model for gravity waves: Formulation and preliminary results for the middle atmosphere. *J. Atmos. Sci.,* **52,** 1959–1984.

Marti, J., and K. Mauersberger, 1993: A survey and new measurements of ice vapor-pressure at temperatures between 170 and 250 K. *Geophys. Res. Lett.,* **20,** 363–366.

McCormack, J. P., and Coauthors, 2004: NOGAPS-ALPHA model simulations of stratospheric ozone during the SOLVE2 campaign. *Atmos. Chem. Phys.,* **4,** 2401–2423.

Nance, L. B., 1997: On the inclusion of compressibility effects in the Scorer parameter. *J. Atmos. Sci.,* **54,** 362–367.

——, and D. R. Durran, 1994: A comparison of the accuracy of three anelastic systems and the pseudo-incompressible system. *J. Atmos. Sci.,* **51,** 3549–3565.

Newman, P. A., and E. R. Nash, 2000: Quantifying the wave driving of the stratosphere. *J. Geophys. Res.,* **105,** 12 485–12 498.

——, and Coauthors, 1996: Measurements of polar vortex air in the midlatitudes. *J. Geophys. Res.,* **101,** 12 879–12 892.

——, D. W. Fahey, W. H. Brune, M. J. Kurylo, and S. R. Kawa, 1999: Photochemistry of Ozone Loss in the Arctic Region in Summer (POLARIS): Preface. *J. Geophys. Res.,* **104,** 26 481–26 495.

——, E. R. Nash, and J. E. Rosenfield, 2001: What controls the temperature of the Arctic stratosphere during spring? *J. Geophys. Res.,* **106,** 19 999–20 010.

——, and Coauthors, 2002: An overview of the SOLVE/THESEO 2000 campaign. *J. Geophys. Res.,* **107,** 8259, doi:10.1029/2001JD001303.

Pagan, K. L., A. Tabazadeh, K. Drdla, M. E. Hervig, S. D. Eckermann, E. V. Browell, M. J. Legg, and P. G. Foschi, 2004: Observational evidence against mountain-wave generation of ice nuclei as a prerequisite for the formation of three NAT PSCs observed in the Arctic in early December 1999. *J. Geophys. Res.,* **109,** D04312, doi:10.1029/2003JD003846.

Parrish, D. F., and J. C. Derber, 1992: The National Meteorological Center's spectral statistical-interpolation analysis scheme. *Mon. Wea. Rev.,* **120,** 1747–1763.

Pawson, S., and B. Naujokat, 1999: The cold winters of the middle 1990s in the northern lower stratosphere. *J. Geophys. Res.,* **104,** 14 209–14 222.

Pyle, J. A., and N. R. P. Harris, 1995: Lessons for the future from coordinated European stratospheric campaigns. *Phys. Chem. Earth,* **20,** 5–12.

Randel, W. J., and F. Wu, 1999: Cooling of the Arctic and Antarctic polar stratospheres due to ozone depletion. *J. Climate,* **12,** 1467–1479.

Sawyer, J. S., 1962: Gravity waves in the atmosphere as a three-dimensional problem. *Quart. J. Roy. Meteor. Soc.,* **88,** 412–425.

Schoeberl, M. R., 1985: The penetration of mountain waves into the middle atmosphere. *J. Atmos. Sci.,* **42,** 2856–2864.

Schulz, A., and Coauthors, 2001: Arctic ozone loss in threshold conditions: MATCH observations in 1997/1998 and 1998/1999. *J. Geophys. Res.,* **106,** 7495–7503.

Scott, S. G., T. P. Bui, K. R. Chan, and S. W. Bowen, 1990: The meteorological measurement system on the NASA ER-2 aircraft. *J. Atmos. Oceanic Technol.,* **7,** 525–540.

Shepherd, T. G., 2000: The middle atmosphere. *J. Atmos. Sol. Terr. Phys.,* **62,** 1587–1601.

Shutts, G. J., 1998: Stationary gravity-wave structure in flows with directional wind shear. *Quart. J. Roy. Meteor. Soc.,* **124,** 1421–1442.

Skamarock, W. C., 2004: Evaluating mesoscale NWP models using kinetic energy spectra. *Mon. Wea. Rev.,* **132,** 3019–3032.

Skeie, P., and S. Grønås, 2000: Strongly stratified easterly flows across Spitzbergen. *Tellus,* **52A,** 473–486.

Solomon, S., 1999: Stratospheric ozone depletion: A review of concepts and history. *Rev. Geophys.,* **37,** 275–316.

Sparling, L. C., A. R. Douglass, and M. R. Schoeberl, 1998: An estimate of the effect of unresolved structure on modeled ozone loss from aircraft observations of CIO. *Geophys. Res. Lett.,* **25,** 305–308.

Stefanutti, L., A. R. MacKenzie, S. Balestri, V. Khattatov, G. Fiocco, E. Kyro, and T. Peter, 1999a: Airborne Polar Experiment/Polar Ozone, Lee-waves, Chemistry and Transport (APE/POLECAT): Rationale, road map and summary of measurements. *J. Geophys. Res.,* **104,** 23 941–23 959.

——, L. Sokolov, S. Balestri, A. R. MacKenzie, and V. Khattatov, 1999b: The M-55 Geophysica as a platform for the Airborne Polar Experiment. *J. Atmos. Oceanic Technol.,* **16,** 1303–1312.

Svendsen, S. H., N. Larsen, B. Knudsen, S. D. Eckermann, and E. V. Browell, 2005: Influence of mountain waves and NAT

nucleation mechanisms on polar stratospheric cloud formation at local and synoptic scales during the 1999–2000 Arctic winter. *Atmos. Chem. Phys.,* **5,** 739–753.

Swinbank, R., R. L. Orris, and D. L. Wu, 1999: Stratospheric tides and data assimilation. *J. Geophys. Res.,* **104,** 16 929–16 941.

Toon, O. B., R. P. Turco, J. Jordan, J. Goodman, and G. Ferry, 1989: Physical processes in polar stratospheric ice clouds. *J. Geophys. Res.,* **94,** 11 359–11 380.

Tsias, A., and Coauthors, 1999: Aircraft lidar observations of an enhanced type Ia polar stratospheric clouds during APE-POLECAT. *J. Geophys. Res.,* **104,** 23 961–23 969.

Tuck, A. F., R. T. Watson, E. P. Condon, J. J. Margitan, and O. B. Toon, 1989: The planning and execution of ER-2 and DC-8 aircraft flights over Antarctica, August and September 1987. *J. Geophys. Res.,* **94,** 11 181–11 222.

Voigt, C., and Coauthors, 2000: Non-equilibrium compositions of liquid polar stratospheric clouds in gravity waves. *Geophys. Res. Lett.,* **27,** 3873–3876.

Vosper, S. B., 2003: Development and testing of a high resolution mountain-wave forecasting system. *Meteor. Appl.,* **10,** 75–86.

——, and R. M. Worthington, 2002: VHF radar measurements and model simulations of mountain waves over Wales. *Quart. J. Roy. Meteor. Soc.,* **128,** 185–204.

Waugh, D. W., J. M. Sisson, and D. J. Karoly, 1998: Predictive skill of an NWP system in the southern lower stratosphere. *Quart. J. Roy. Meteor. Soc.,* **124,** 2181–2200.

Webster, P. J., and R. A. Houze Jr., 1991: The Equatorial Mesoscale Experiment (EMEX): An overview. *Bull. Amer. Meteor. Soc.,* **72,** 1481–1506.

Wirth, M., and Coauthors, 1999: Model guided Lagrangian observation and simulation of mountain polar stratospheric clouds. *J. Geophys. Res.,* **104,** 23 971–23 981.

Wofsy, S. C., R. C. Cohen, and A. L. Schmeltekopf, 1994: Overview: The Stratospheric Photochemistry Aerosols and Dynamics Expedition (SPADE) and Airborne Arctic Stratospheric Expedition II (AASE II). *Geophys. Res. Lett.,* **21,** 2535–2538.